USE OF METAL TEMPLATES FOR MICROCAVITY FORMATION IN ALUMINA

A Thesis Submitted to
the Graduate School of Engineering and Sciences of
İzmir Institute of Technology
in Partial Fulfillment of the Requirements for the Degree of

MASTER OF SCIENCE

in Materials Science and Engineering

by
Sırma BALKAN

December 2011
İZMİR

We approve the thesis of **Sırma BALKAN**

_____
Prof. Dr. Sedat AKKURT
Supervisor

_____
Prof. Dr. Muhsin ÇİFTÇİOĞLU
Committee Member

_____
Prof. Dr. Fehime ÖZKAN
Committee Member

19 December 2011

_____   _____
Assoc. Prof. Dr. Mustafa M. DEMİR   **Prof. Dr. R. Tuğrul SENGER**
Head of the Department of Materials   Dean of the Graduate School of
Science and Engineering   Engineering and Sciences

ACKNOWLEDGEMENTS

ABSTRACT

USE OF METAL TEMPLATES FOR MICROCAVITY FORMATION IN ALUMINA

Alumina ceramics with microtunnels are produced by compressing submicron sized alumina powder and Ti, Cu or stainless steel wires in a metal die before firing the compacts at $1350^{o}C$ for 4 hours. Diameters of wires ranged from 50 to 125 micrometers. Copper was found to completely melt and flow away from the compact leaving no trace of copper in alumina. Stainless steel diffused out into the alumina leaving few pores behind. Titanium, on the other hand, diffused into alumina at 20 to 30micrometers/hour and left plenty of Kirkendal porosity behind. The amount of porosity could have been increased further by applying intensive milling to the powder. But no milling was done in this study and hence a complete micro-tunnel was not obtained. The Kirkendal effect was observed to be effective in producing pores in the ceramic. Densification behavior of the ceramic was also investigated with a vertical dilatometer. Densities up to 93% were achieved in the ceramics. In some tests Ti metal plates were used as diffusion couples with alumina compacts. Similar diffusion behavior was observed with plates and wires.

ÖZET

ALÜMİNA İÇİNDE MİKROBOŞLUK OLUŞTURULMASI İÇİN METAL ŞABLONLAR KULLANILMASI

Mikro tüneller içeren alümina seramikler, mikron altı boyutlu alümina tozu ile titanyum, bakır ya da paslanmaz çelik tellerin metal bir kalıp ile sıkıştırılarak $1350^{o}C$ sıcaklıkta 4 saat pişirilmesi ile üretilmiştir. Tellerin çapları 50 ile 125 mikrometre arasında değişmektedir. Bakır, tamamen eriyik halde bulunmuş ve alümina içerisinde hiçbir iz bırakmadan akıp gitmiştir. Paslanmaz çelik ise gerisinde biraz gözenek bırakarak alümina içine difüze olmuştur. Öte yandan titanyum, alümina içine 20-30 mikrometre/saat hızla difüze olmakta ve arkasında fazlaca Kirkendall porozite kalıntısı bırakmaktadır. Gözeneklilik miktarı, tozlara yoğun öğütme uygulanarak daha da arttırılabilir. Fakat bu çalışmada öğütme kullanılmamıştır ve bu yüzden tam bir mikro tünel gözlenmemiştir. Seramiklerde oluşan gözeneklerde Kirkendall etkisi yoğun bir biçimde gözlenmiştir. Ayrıca seramiğin yoğunlaşma davranışı dikey dilatometre ile incelenmiştir. Seramiklerde % 93'e varan yoğunluk elde edilmiştir. Bazı testlerde, metal Ti plakalar, yoğunlaştırılmış alümina ile difüzyon çifti olarak kullanılmaktadır. Benzer difüzyon davranışı plaka ve teller kullanılarak da gözlenir.

TABLE OF CONTENTS

LIST OF FIGURES

LIST OF TABLES

CHAPTER 1

INTRODUCTION

Porous oxide ceramics are important for a variety of applications such as thermal insulation, filtration, biomedical and catalyst substrates. Porous ceramics take advantage of the already low density of many ceramics extending their application to even lower weight restrictions, while commonly sacrificing loss in strength (Gibson et al., 1986). Alumina (Al_2O_3) is a stable and very strong bioceramic which, when doped with magnesium, calcium and phosphate ions, can potentially combine bioactivity with high porosity and high strength.

Alumina has been used as a biomaterial for an extensive period of time with its biocompatibility well documented by many researchers in past decades. Alumina, a bioinert material demonstrates exceptional stability in the physiological environment with properties of excellent corrosion and wear resistance. It has been used in a wide range of applications from dental and maxillofacial applications to compressive load-bearing and wear-resistant applications in orthopaedics (Soh et al., 2009).

High density in alumina components is normally achieved by sintering compacted alumina powder above 1200 to 1700ºC depending on the surface area of the powder. Nevertheless, many of the metals used in these applications have melting points near or below the generally desired sintering temperature of alumina (such as Ti with 1668ºC and stainless steel with ~1400ºC). On the other hand, the importance of porous materials has increased with emerging technologies.

Titanium, stainless steel, copper and alumina are used widely in the industrial and biomedical applications. Combination of Ti–Al_2O_3, stainless steel-Al_2O_3 and copper-Al_2O_3 are recently accepted as advanced engineering materials with encouraging performance. These combinations of metals and ceramics have pleasant properties, such as low density, excellent oxidation and corrosion resistance, adequate creep resistance at high temperature, good wear resistance and high hardness (Fan et al., 2006).

The aim of this thesis, is to produce alumina ceramics containing tailored micro-tunnels. For this purpose, a variety of high-purity alumina powders and small diameter metal wires embedded in alumina were used as templates. When the compact is heated

at around 1350°C the metal oxidizes and the metal ions diffuse out into the alumina matrix. A counterdiffusion of Al^{+3} ions occurs in reverse direction. But the former is faster due to higher ionic mobility of the Ti^{+4} ions. The misbalance in the diffusion rates of the two components leads to the formation of pores behind Ti^{+4} ions. This effect was first recognized by Smigelkas and Kirkendal in 1947 and hence is named the Kirkendal effect (Kirkendall et al., 1947). In the late 1940s, Kirkendall explored that the interface between copper and zinc in brass moved at an elevated temperature due to their different diffusion rates. This rare occurence was later called as the Kirkendall effect. Porous materials, which contain micro-pores, can be created with combination of metal templates-Al$_2$O$_3$ in the alumina structure. In this case, the importance of the diffusion is great with Kirkendall effect.

The Kirkendall effect derives from the difference in exclusive diffusional movability between the two elements of a binary diffusion couple. As a result of diffusion with Kirkendall effect at high temperatures, the formation of new phases (such as Al$_2$TiO$_5$) are most likely to occur in the material interface.

Goodshaw and his research team (Goodshaw et al., 2009) investigated the microcavity formation conditions, mechanism and kinetics in alumina using Ti templates. They emphasized the importance of sintering temperature and diffusion for the creation of microcavity.

Buscaglia and Carry (Buscaglia et al., 1993) examined reaction sintering of aluminium titanate (Al$_2$TiO$_5$). The mechanism of Al$_2$TiO$_5$ formation from the starting oxides Al$_2$O$_3$ and TiO$_2$ has been carefully investigated by Freudenburg and Mocellin (Freudenburg and Mocellin, 1987-1988), who have underlined the importance of the nucleation and growth process microstructure in the temperature range 1280-1400°C.

In this thesis, densification behavior and specific surface area (BET) of different alumina powders and SEM observations of the alumina samples, that contain metal templates were investigated. Ceramic materials are inert and resistant to corrosion.

In Chapter 2 of this thesis, a description of the porous materials, properties and applications of materials, biomedical materials and the Kirkendall effect, its scope and a theory of BET, Archimedes density measurement and densification rate will be presented. The experimental procedure and the results of this study are given and discussed in Chapters 3 and 4, while the conclusions are stated in the last chapter.

CHAPTER 2

LITERATURE REVIEW

2.1. Porous Materials

Porous materials refer to solids possessing pores. The porosity is the fraction of the pore volume to the total volume. Pores inside the solids can be classified into open pores and closed pores. Open pores are connected to the outside of the material surface and can be penetrated by fluids; closed pores are isolated holes.

Porous ceramics are used for many special engineering applications. Their specific structural properties make them perfect materials for some applications. Especially thier high separation efficiency, non-corrosive structures and thermal resistance as well as mechanical strength and structural stability makes them very efficient materials for engineering applications (Dong and Diwu, 2007). Moreover porous ceramics have low mass density, high chemical saturation and resistance to abrasion. The other causes of preference for porous ceramics for engineering ceramics are the abundance of low-cost source of raw materials (Erol, 2008).

Characteristic properties of porous ceramics make them suitable for different applications like: filters for molten metals and hot gases, refractory linings for furnaces, and porous implants in the area of biomaterials (Sepulveda and Binner, 1999), thermal coatings, human bone substrates. (Sadowski and Samborski, 2007). And also porous ceramics are widely used as catalyst carriers, separation membranes and diffusers (Isobe and Tomita1, 2006).

2.2. Properties and Applications of Alumina (Al_2O_3)

Alumina is a widespread component of siliceous minerals. It often occurs as single crystal in the form of sapphire and ruby and in large deposits as the hydrated oxide bauxite ($Al_2O_3 \cdot H_2O$) (McColm, 1983).

The Bayer process is the main technique used for the industrial production of α-alumina. Bauxite, naturally contaminated with other oxides, is used as a starting material in the Bayer process (Moulson and Herbert, 1990). This involves raw material preparation, digestion, clarification, precipitation and calcination. Practically all the powder for the fabrication of alumina ceramics is prepared using this technique. A purer alumina product can be made by preparing ammonium alum ($NH_4Al(SO_4)_2) \cdot 12H_2O$) (Liu, 2011).

Among the aluminium oxide, α-alumina is thermally the most stable phase. For example, γ-alumina will convert to α-alumina above 1000ºC. α-alumina has a hexagonal structure and two alumina molecules per unit, as shown schematically in Figure 2.1. Three oxygens form an equilateral triangle with aluminiums above and below the centre of the triangle. One of these groups is placed at each corner of a cube while another is placed at the centre of the cube.
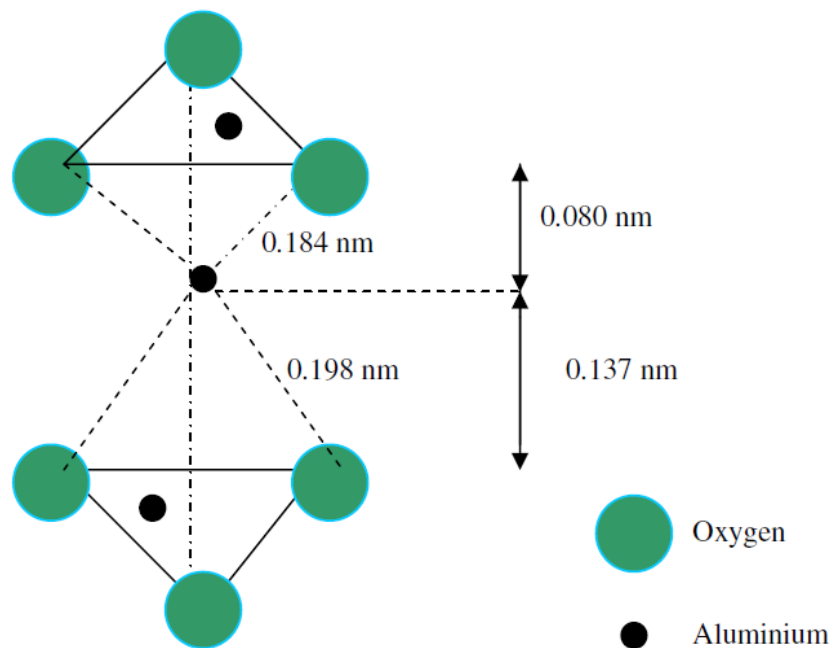
Figure 2.1. Schematic illustration of oxygen arrangement around Al^{3+} ion in alumina
(Source: McColm, 1983).

Alumina ceramic is one of the most widely studied and used advanced ceramic materials. Table 2.1 shows properties of alumina. Some selected properties of sintered α-alumina are shown in Table 2.2 (The purity of listed α- alumina is at least 99.5% and the density is at least 98% of the theoretical density. The nominal grain size is normally 5 µm). The crystal structure of corundum is illustrated in Figure 2.2. Structures and lattice parameters of stable alumina (corundum) and unstable aluminas are listed in Table 2.3.

Table 2.1. Properties of alumina
(Source: Insaco Inc., 2006)

Property	Value
Density (g/cm^3)	3.9
Hardness (Rockwell 45N)	82
Melting Point (^{o}C)	2050
Tensile Strength (Kpsi)	54
Modulus of Elasticity (psi x 10^6)	46
Fracture Toughness (MPa m$^{1/2}$)	4.3
Coefficient of thermal expansion (x10^{-6}/^{o}C)	7.2
Thermal conductivity (W/m^{o}K)	30.3
Volume resistivity (Ω-cm^2/cm)	>10^{14}

Table 2.2. Some properties of sintered α-alumina
(Source: Claussen, 1976).

Property	Temperature ^{o}C					
	20	500	1000	1200	1400	1500
Bulk density (g/cm^3)	3.984	3.943	3.891	3.868	3.845	3.834
Compressive strength (GPa)	3.0	1.6	0.7	0.4	0.3	0.28
Flexural strength (MPa)	380	375	345	300	210	130
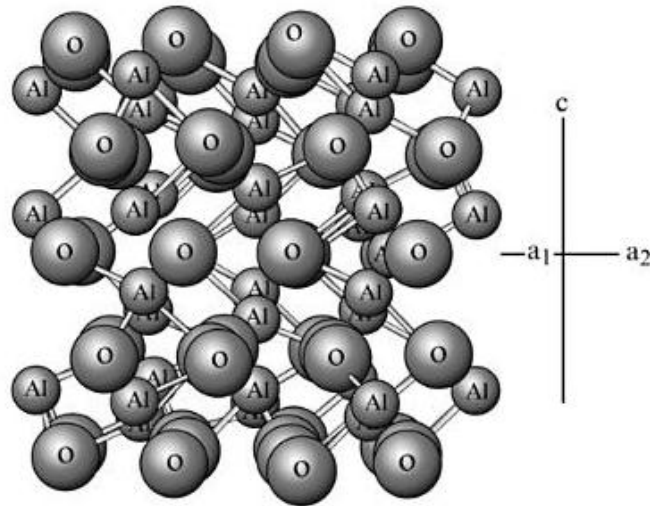
Figure 2.2.   The structure of corundum (alpha-alumina). The aluminum atoms occupy two thirds of the octahedral interstices in a hexagonal close-packed array of oxygen atoms, which is distorted because the octahedral share faces in pairs (Source: Shackelford and Doremus, 2008).

Table 2.3. Structures of stable alumina (corundum) and unstable aluminas
(Source: Shackelford and Doremus, 2008).

Designation	Structure	Lattice Parameters, angle (Å)		
		a	b	c
Corundum	Hexagonal (rhombohedral)	4.758		12.991
Beta	Cubic (spinel)	7.90		
Gamma	Tetragonal	7.95		7.79
Delta	Tetragonal	7.97		23.47
Theta	Monoclinic	5.63	2.95	11.86 103° 42'
Kappa	Orthorombic	8.49	12.73	13.39

The relative abundance and low cost of the materials resource is an additional benefit for commercial application. Alumina ceramics share with other advanced ceramics the characteristics of high-temperature stability and the retention of strength at high temperatures. Alumina ceramics can be utilized wherever exceptionally good dielectric properties, high mechanical strength, and high thermal conductivity are needed, such as for microwave windows, cutting tools, and spark plug insulation. Moreover, high-density, high-purity (>99.5%) Al_2O_3 (α-alumina) was the first bioceramic widely used clinically (Hench, 1998).

2.3. Properties and Applications of Titanium, Stainless Steel and Copper

2.3.1. Titanium

Titanium is an allotropic element; that is, it exists in more than one crystallographic form. The Kroll process is the method used to refine titanium ore to metallic titanium (Lautenschlager and Monaghan, 1993). At room temperature, titanium has hexagonal close-packed (HCP) crystal structure, which is referred as "alpha" (α) phase. On heating this structure transforms to a body-centered cubic (BCC) crystal structure, called "beta" (β) phase at 882.5° C (Kotian, 2011). Figure 2.3 shows crystal structure of HCP α and BCC β phase. Table 2.4 gives lattice parameters of titanium at room temperature.
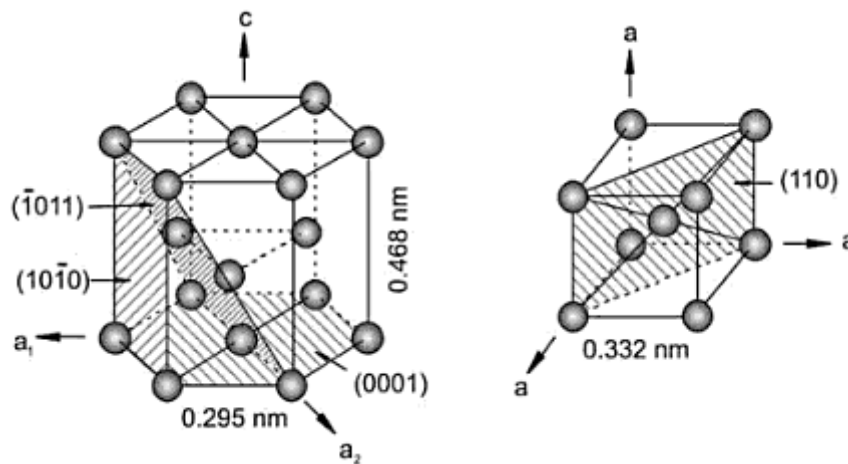
Figure 2.3. Crystal structure of HCP α and BCC β phase
(Source: Leyens et al., 2003)

Table 2.4. Room temperature lattice parameters of titanium
(Source: Murray, 1987).

Crystal Structure	Lattice Parameters		
	a (nm)	c (nm)	c/a
HCP	0.295	0.468	1.587

Commercially pure (CP) titanium and titanium alloys have wide range of applications in aerospace, energy, chemical and automotive industries. Some of the titanium alloys are excellent materials for biomedical use, especially as orthopedic and dental alloys. The most important characteristic features of these biomedical titanium and its alloys are high strength, low density, excellent corrosion resistance and the best biocompatibility among metallic materials (Kotian, 2011). Table 2.5 shows some properties of titanium.

Table 2.5. Some properties of titanium
(Source: Collings, 1994).

Property	Titanium
Density (g/cm^3) at 20°C	4.51
Melting Temperature (^{o}C)	1670 ± 5
Coefficient of Thermal Expansion (1/ ^{o}C) at 20°C	8.41 x 10^{-6}
Thermal Conductivity (W/m.^{o}C)	17

2.3.2. Stainless Steel

Stainless Steels are alloy of iron and carbon that contain chromium ranging from 10.5 − 11.5% (Ramlee, 2008). Usually, stainless steels contain less than 30% Cr and more than 50% Fe. The chromium content is the secret to the stain-resisting properties (Ramlee, 2008). Chromium inhibits corrosion and thus plays a part defining stainless steel. In the presence of oxygen, chromium-rich oxide surface film is formed on the surface in the form of chromium (III) oxide (Cr_2O_3) (Ramlee, 2008). This layer is too thin to be visible, meaning that the metal stays shiny. This is the reason of why they attain their stainless characteristics. In fact, the more chromium, the more corrosion-resistance of the stainless steel behaves. But chromium is not the only factor in corrosion resistance (Ramlee, 2008). Additions of many other alloying elements enhance the properties of a particular grade and type of stainless steel including nickel (Ni), molybdenum (Mo), copper (Cu), titanium (Ti), aluminum (Al), silicon (Si), niobium (Nb) and nitrogen (N).

Selection of stainless steels based on the corrosion resistance, fabrication characteristics, availability, mechanical properties in specific temperature ranges and product cost. However, corrosion resistance and mechanical properties are usually the most important factors in selecting a grade for a given application.

Crystal structure of stainless steel is face centered cubic (FCC) (Figure 2.4). The lattice parameters of stainless steel are given in Table 2.6 and Table 2.7 shows some properties of stainless steel.
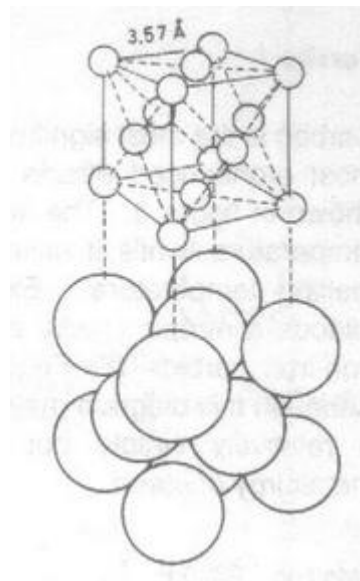
Figure 2.4. Crystal structure of austenite (FCC)
(Source: Oocities, 2011).

Table 2.6. Crystal structure and lattice parameter of stainless steel
(Source: Marshall, 1984).

Phase	Crystal Structure	Lattice Parameter (Å)
Austenite	FCC	$a_o = 3.598$

Table 2.7. Some properties of stainless steel (316L)
(Source: Ramlee, 2008).

Property	Stainless Steel
Density (g/cm^3)	7.9
Melting Temperature (^{o}C)	1350
Thermal Conductivity (BTU/Ft^2/Ft/Hr/°F) 100°C	9.4
Coefficient of Thermal Expansion (Per°Fx10^{-6}) 0-100°C	8.9

Austenitic stainless steels are frequently used in biomedical applications, such as orthopedic implants, due to properties like high corrosion and fatigue resistance as well as high fracture toughness. In addition to biocompatibility, these properties are important in the selection and adaptation of a material for biomedical applications (Mariotto et al., 2011).

2.3.3. Copper

Copper is included in the first sub-group of the periodic table, together with silver and gold. The microstructure of pure copper consists of a homogeneous phase and crystallizes in a face centred cubic lattice (Figure 2.5). The lattice constant of copper crystal structure is given in Table 2.8. Some physical properties of pure copper are illustrated in Table 2.9.
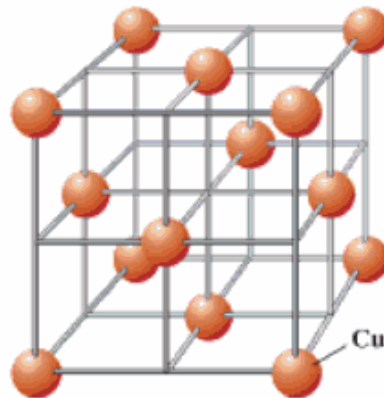
Figure 2.5. Crystal structure and crystal lattice of copper
(Source: Ebbing and Gammon, 2010).

Some physical properties of copper depend heavily on the purity or the contamination. On the other hand there is the possibility of changing certain physical properties over a wide range by alloying the metals and by hot/or cold working or heat treatment (Lipowsky and Arpaci, 2008). In this way, many characteristics of the copper materials can be adapted to the respective application.

Table 2.8. Crystal structure and lattice parameter of copper
(Source: (Lipowsky and Arpaci, 2008)).

Phase	Crystal Structure	Lattice Parameter (nm)
Copper	FCC	$a_o = 0,3608$

Table 2.9. Some physical properties of pure copper at 20^oC
(Source: Lipowsky and Arpaci, 2008).

Property	Copper
Density at 1083^oC, solid (g/cm^3)	8.32
Density at 1083^oC, liquid (g/cm^3)	7.99
Melting point (^oC)	1083
Electrical conductivity at RT (MS/m)	59.62
Specific electrical resistance at RT ($\mu\Omega$.cm)	1.67

The applications of copper are in electrical wires , roofing and plumbing, dental amalgam, implant and industrial machinery. Copper is mostly used as a metal, but when a higher hardness is required it is combined with other elements to make an alloy (5% of total use) such as brass and bronze (Emsley, 2003).

2.4. Metal - Oxide Bi-materials

Bi-materials are composed of at least two layers which are made of different materials and compositions. They have functional properties, depending on mechanical, electrical and magnetic properties of their components (Yalamaç, 2010). Their application areas range from electronic packaging applications such as multi-layer ceramic capacitors to thin film-substrate systems used widely in the microelectronics

industry (Boonyongmaneerat and Schuh, 2006). Production of the bi materials by different methods and with various components is an interesting subject for the researchers.

Many researchers studied metal-oxide systems (Boonyongmaneerat and Schuh, 2006; Tummala, 1988; Kohl, 1964). The application of diffusion bonding to ceramic-metal systems is more recent and theoretical modelling has yet to be developed, although Derby (1986) has suggested Al grain boundary diffusion to control Al_2O_3-Al bonding.

Boonyongmaneerat and Schuh investigated tungsten(W)/alumina(Al_2O_3) metal-oxide bilayers. According to their study, A two-layer compact joining specimen was the test geometry chosen for this work, for reasons that will become clear in the next section. To prepare such specimens, Al_2O_3 and W powder were sequentially loaded into a die of rectangular cross-section and cold pressed without binders using a single-action press at 80 MPa. These green specimens were then co-fired in a furnace at $1177^{o}C$ for 1 hour, followed by slow furnace cooling. It has been found that no primary chemical interaction occurs along the W/Al_2O_3 interface, and mechanical interlocking is the main mechanism that controls adhesion.

Figure 2.6 (a) and (b) shows the test specimens, a magnified view of the interfacial region between W and Al_2O_3 is shown in a scanning electron micrograph.
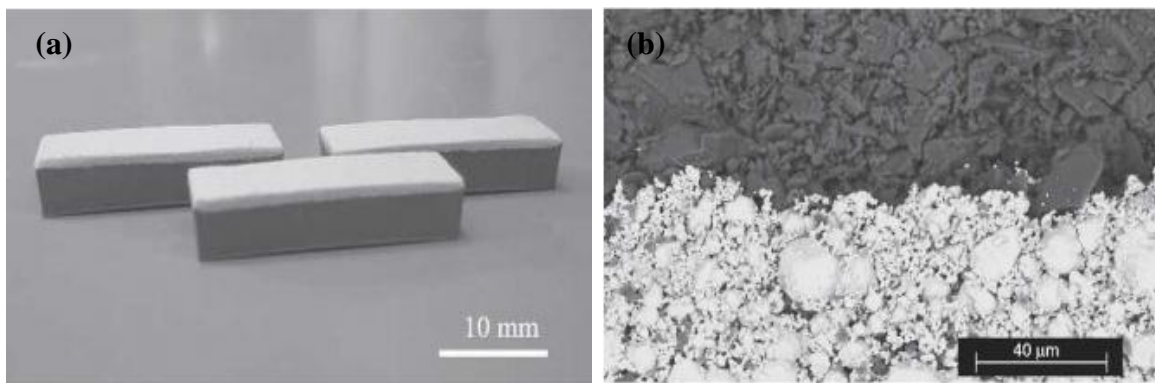
Figure 2.6. W/Al_2O_3 bilayer specimens, (a) a macroscopic view and (b) a micrograph of the interfacial region (Source: Boonyongmaneerat and Schuh, 2006).

Goodshaw et al. (2009) studied formation condition in Ti–TiO_2 and Ti–ZrO_2 systems. In Figure 2.7 (a) the lack of contrast between the Ti wire and the TiO_2 matrix indicates that the wire has most likely completely oxidized to form TiO_{2-x} by absorption

of some of the oxygen from the air or the matrix. This would explain the annular cavity that has formed around the original wire (Goodshaw et al., 2009). It appears unlikely that the Ti–TiO$_2$ system will enable shaped microcavity formation. The Ti wire in milled ZrO$_2$ powder did not form a cylindrical cavity either, however, an interesting sponge-like microstructure has developed with fine ligands connecting the wire remnant to the surrounding ZrO$_2$ (Goodshaw et al., 2009).
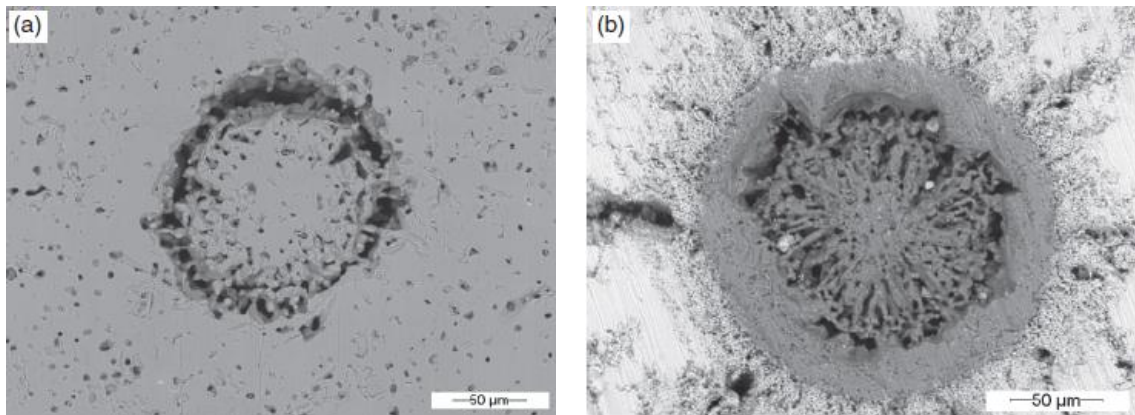
Figure 2.7 (a) Ti–TiO$_2$ system (b) Ti–ZrO$_2$ system
(Source: Goodshaw et al., 2009).

2.5. Diffusion and Kirkendall Effect

Diffusion test is a useful and common technique to understand the growth of intermediate new phases between the two end components which were previously shaped and sintered to some extent. It has been used by many researchers (Goodshaw et al., 2009; Buscaglia et al., 1997; Siao et al., 2009) in the literature.

One of the most significant experiments in the field of solid state diffusion was conducted by Smigelkas and Kirkendall in 1947 (Smigelkas and Kirkendall, 1947). In the experiment by Smigelkas and Kirkendall, a rectangular bar (18×1.9 cm^2) of 70-30 wrought brass (70wt%Cu-30wt%Zn) was taken. This bar was ground and polished and then 130 μm diameter molybdenum wires, which are inert to the system, were placed on opposite sides of the surfaces. Then a copper layer of 2500 μm was deposited on that, as shown in Figure 2.8. This couple was subjected to annealing at 785 °C. After annealing for a certain time one small piece was cross-sectioned to examine and the rest of the part was annealed further. Following this method, it was possible to get

specimens at different annealing times. With annealing, α-brass grows in between and after etching, the distance between the markers was measured. If the diffusivities of copper and zinc are the same and there is no change in volume during diffusion/reaction, marker should not move and stay at the original position.

However, after measuring, it was clear that with increasing annealing time, the distance between markers decreases parabolically with time. Considering the change in the lattice parameter, it was found that only $1/5^{th}$ of the displacement occurred because of molar volume change (Paul, 2004). This shift was explained as Kirkendall effect. When initial interface is shifting, diffusion porosity may develop and locate in the side containing faster moving atom (Siao et al., 2009).

From this study two conclusions were drawn which had enormous impact at that time on solid-state diffusion:

1. The rate of diffusion of zinc is much greater than that of copper in alpha brass, and

2. When zinc diffuses more rapidly then copper in alpha brass, the interface shifts to compensate at least partially for the diffusion rate (Paul, 2004).
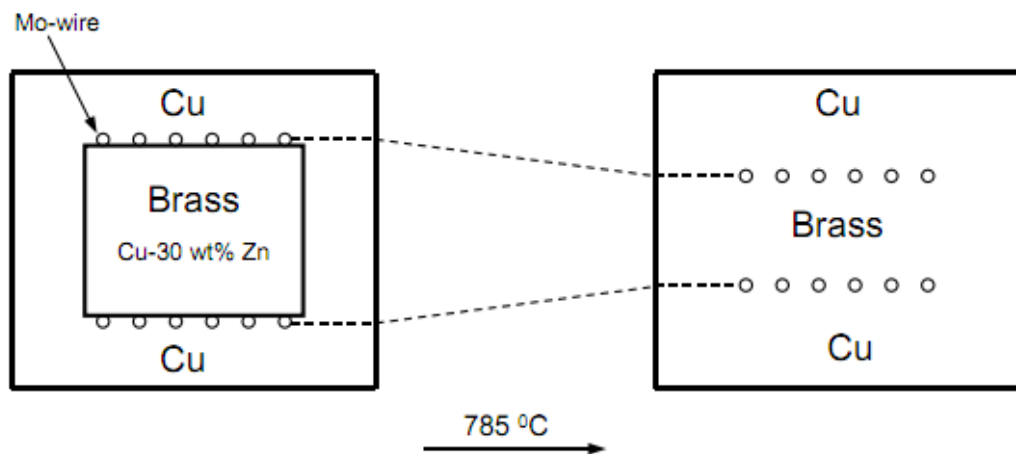
Figure 2.8.   Schematic representation of cross-section of the diffusion couples before and after annealing at 785°C (Source: Smigelkas and Kirkendall, 1947).

Till then, direct exchange or ring mechanisms were accepted as diffusion mechanism in the solid-state as shown in Figure 2.9. If any of these mechanisms would be true then diffusivities of the species should be the same. However, from the Kirkendall's experiment, it is evident that Zn diffuses faster than Cu, which results into the movement of the markers (Paul, 2004). When zinc diffuses away, all the sites are

not occupied by the flow of Cu from opposite direction and because of that vacant sites are left unoccupied. In other sense, there should be a flow of vacancies opposite to the faster diffusing species Zn to compensate for the difference between the Zn and Cu flux. Vacancies will flow towards the brass side and excess Zn will diffuse towards the Cu-side. Ultimately, this results into shrinking in the brass side and swelling in the copper side so that markers move to the brass side. In some diffusion reactions pores can be found in the product phase (Paul, 2004). If there is not enough plastic relaxation during the process, vacancies will coalesce to form pores or voids in the reaction layer.

From this experiment, it was clear that diffusion occurs by a vacancy mechanism and after that the direct exchange and ring mechanisms were abandoned. At first this work was highly criticized but later this phenomenon was confirmed from experiments on many other systems (Silva and Melh, 1951). Readers, interested on the historical developments are advised to read the article by Nakajima (Nakajima, 1997) and da Silva followed by comments from Kirkendall (Silva, 1998). In fact, five years before Kirkendall's publication, Huntington and Seitz (Huntington and Seitz, 1942) already showed that diffusion occurs by the vacancy mechanism, not by direct exchange, but at that time this work was overlooked.
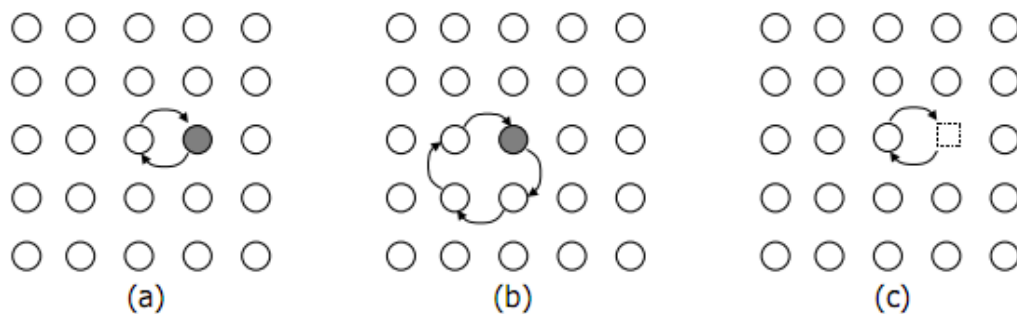
Figure 2.9. Atomic diffusion mechanisms (a) direct exchange mechanism
(b) ring mechanism and (c) vacancy mechanism (Source: Paul, 2004).

2.6. Model for Diffusion between Oxides

In this section diffusion between oxides is explained. In this thesis the following diffusion processes are studied: Al_2O_3-TiO_2, Al_2O_3-CuO, Al_2O_3-$(Fe,Cr)_2O_3$. When the diffusion between TiO_2 and Al_2O_3 is investigated at 1350^oC for 4 hours a concentration profile as shown in Figure 2.10 can be expected.
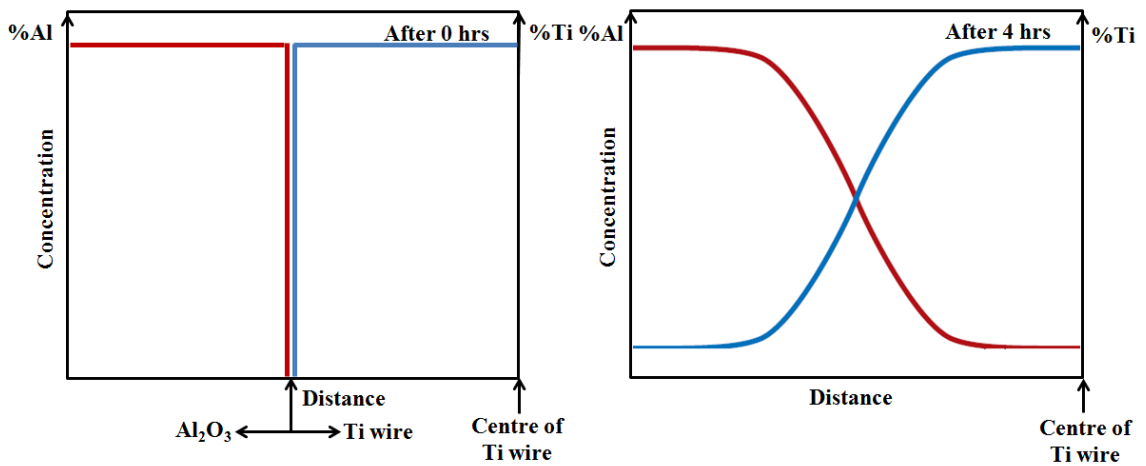
Figure 2.10. Concentrations of Al_2O_3 and Ti as a function of diameter across the couple.

According to Figure 2.10, concentration of Al_2O_3 and Ti is stable at after 0 hours. But after 4 hours soaking time, Al_2O_3 and Ti concentrations vary in the opposite direction toward each other. Figure 2.11 (a), (c) and (b), (d) show a Al_2O_3-Ti diffusion couple before and after a high-temperature heat treatment, showing the diffusion zone, and schematic representations of Al^{+3} (red circles) and Ti^{+4} (blue circles) ion locations within the couple.
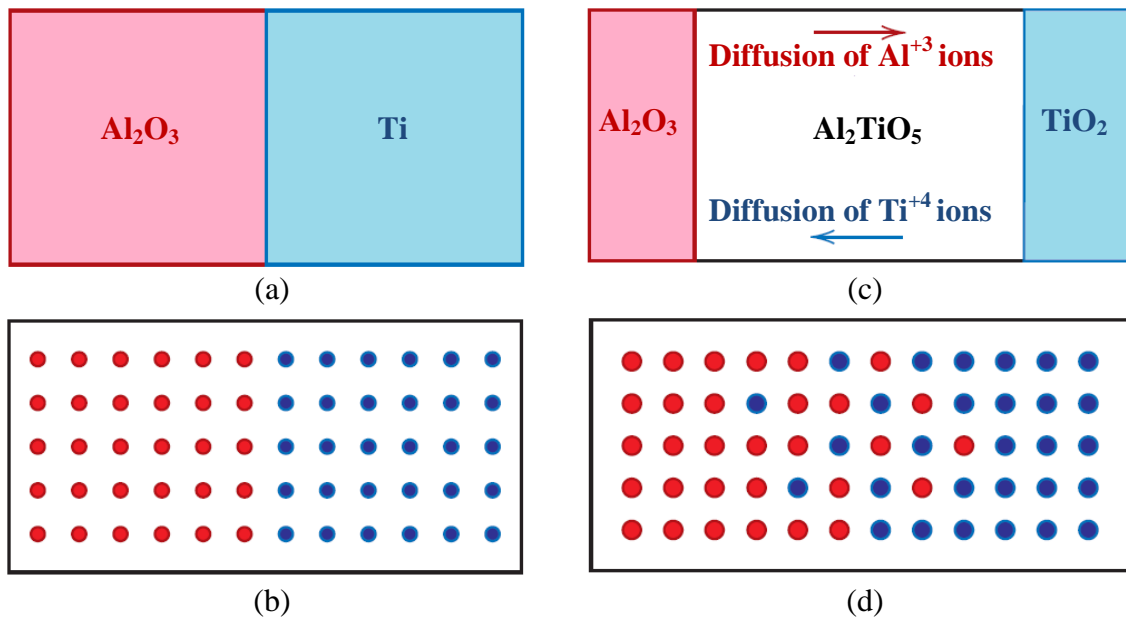
Figure 2.11.   (a), (c) A Al_2O_3-Ti diffusion couple before/after a high-temperature heat treatment, showing the diffusion zone. (b), (d) Schematic representations of Al^{+3} (red circles) and Ti^{+4} (blue circles) ion locations within the couple.

During the 4 hours soaking time at high temperature, the Al^{+3} ions diffuse out into the titanium wire, while Ti^{+4} ions diffuse into the alumina matrix. In the opposite direction, a counterdiffusion occurs with Al^{+3} and Ti^{+4} ions. It is noticed that Ti^{+4} is diffused into the surrounding alumina so the phase of Al_2TiO_5 occured in the middle of the diffusion zone. The diffusion of the Ti^{+4} ions is faster than Al^{+3} ions and the former is faster due to higher ionic mobility of the Ti^{+4} ions. In the diffusion rates of the Al_2O_3 and Ti components, the balance causes the formation of pores on the back of the Ti^{+4} ions. This effect is named the Kirkendal effect (Kirkendall et al., 1939). Figure 2.12 shows the diffusion zone of Al_2O_3-Ti system. Consider the diffusion couple illustrated in Figure 2.13.
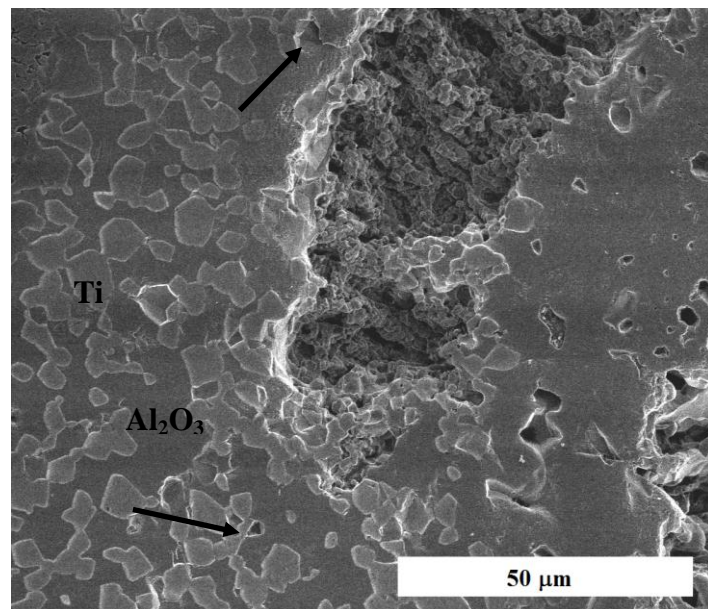
Figure 2.12. The diffusion zone of Al_2O_3-Ti system. Noticed that the arrows indicate the pores.
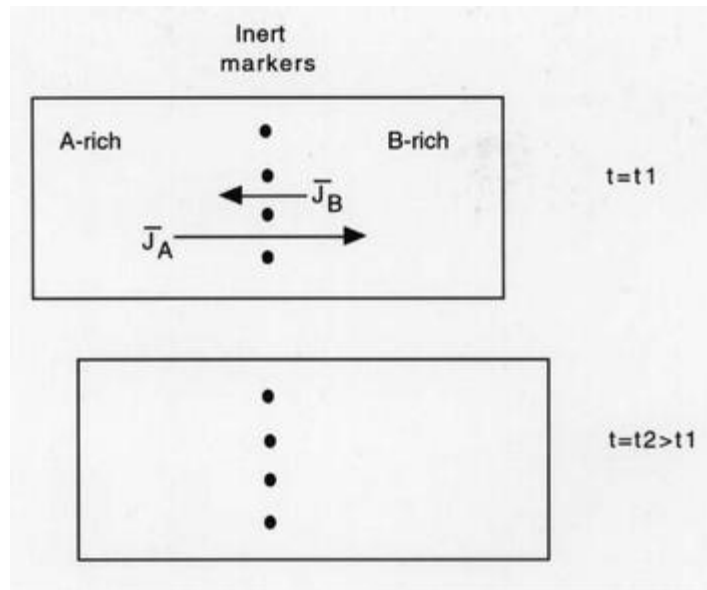
Figure 2.13. Consider the diffusion couple
(Source: Bhadeshia, 2011).

In Figure 2.13, consider the diffusion couple illustrated above, between A and B, where the diffusion rates of the two species are different ($|J_A| > |J_B|$). Since the diffusion fluxes are different, there will be a net flow of matter past the inert markers, causing the couple to shift bodily with respect to the markers. This can only happen if diffusion is by a vacancy mechanism. A place exchange mechanism does not allow the fluxes to be different.

A diffusion couple is created by welding together A and B, with intert markers placed at the weld junction. The markers are in the form of wires extending out of the diffusion couple and attached to the laboratory bench. The whole specimen therefore translates along the bench as diffusion proceeds because the flux of A is larger than that of B. Given that there is a net flow of matter there will be an equal and opposite net flow of vacancies which condense to form pores.

2.7. Densification Rate

The kinetic data for the densification of the powder compact during sintering is important practically and theoretically. They can be obtained as functions of time or temperature by two methods: intermittently, density of compacted powder is measured after firing at the selected temperatures for a determined period of time, continuously,

by the technique of dilatometry (Rahaman, 1995). Shrinkage ($\Delta L/L_o$) is determined from the measured length change in the sample in a dilatometer in comparison to the initial compact size. Computer collected shrinkage and temperature data are accumulated constantly during the heating process (Yalamaç, 2010). Shirinkage reflects the direct action of densification mechanisms like grain boundary diffusion; although simultaneous coarsening processes alter the driving force (Hillman and German, 1992).

Densities, $\rho(T)$, and densification rate curves are computed from the recorded shrinkage data and from final densitiy ρ_f measurements using the following formula (Equation 2.1):

$$\rho(T) \; = \left(\frac{1 + \frac{\Delta L_f}{L_0}}{1 + \frac{\Delta L(T)}{L_0}} \right)^3 \rho_f \tag{2.1}$$

in which L_o is the initial sample length, L_f is the final sample length and $L(T)$ is the sample length at the temperature T (Legros et al., 1999). Final densities were measured by the classical Archimedes method on cooled samples.

To obtain the densification rate, temperature derivative of relative density ρ is taken (Equation 2.2)

$$\frac{d\rho_{(T)}}{dT} \; = \; -3 * \frac{d\left(\Delta L_{(T)}/L_0\right)}{dT} \; * \; \frac{\left(1 + \frac{\Delta L_{(f)}}{L_0}\right)^3}{\left(1 + \frac{\Delta L_{(T)}}{L_0}\right)^4} * \rho_f \tag{2.2}$$

2.8. Archimedes Theory for Density

A standard means to determine the volume of an irregular shape is based on fluid displacement when the component is immersed in a fluid such as water. The measurement must prevent fluid intrusion into surface connected pores to extract an accurate volume. Combined with the dry mass determined prior to the test, a density calculation follows (German and Park, 1946). First, the sample is weighed dry (W_1), then again after oil impregnation of the evacuated pores (W_2), and finally the oil-impregnated sample is immersed in water for the final weight (W_3). Usually a wire is used to suspend the sample in the water and its weight W_w must be measured in water

too. Then the actual of Archimedes density ρ can be calculated from the weight determinations as follows (Equation 2.3):

$$\rho = \frac{W_1 \phi_w}{W_2 - (W_3 - W_W)} \tag{2.3}$$

where ϕ_W is the density of water in kg/m^3, which is temperature dependent as given here (Equation 2.4),

$$\phi_W = 1001.7 - 0.2315T \tag{2.4}$$

with T being the water temperature in ^{o}C. Dividing the measured density by the theoretical density gives the fractional density. One variant uses water impregnation instead of oil to fill the pores, which still involves two immersion events, but there is no oil trapped in the pores (German and Park, 1946).

In Equation 2.3 and 2.4, T is water temperature, W_1 is dry mass of the sample prior to testing, kg, W_2 is wet mas of the sample after filling pores with fluid, kg, W_3 is mass of the component immersed in water, kg, W_W is mass of the suspension wire, kg, ϕ_W is temperature-corrected density of water, kg/m^3 and ρ is component density, kg/m^3.

CHAPTER 3

EXPERIMENTAL

In this chapter, the materials used and the experimental procedure are explained. The thesis is releated to the study of diffusion of titanium wire, titantium plate, copper wire and stainless steel wire into alumina.

3.1. Materials

In this thesis, first a variety of high-purity alumina powders made by different manufacturers (CT3000SG, ALCOA, 99,9%) (AKP50, Sumitomo, 99,9%) (CR6, Baikowski, 99,9%) (CR15, Baikowski, 99,9%) (CR30F, Baikowski, 99,9%) were used to prepare the base materials. The smallest sizes (125μm) of pure titanium (Timet, Turkey) and stainless steel wires (Elsan, Turkey) and titanium plate (Timet, Turkey) were used in order to produce micro-tunnels. Figure 3.1 shows photographs of some of the as-received samples. Below are given the properties of the starting powders (Table 3.1).
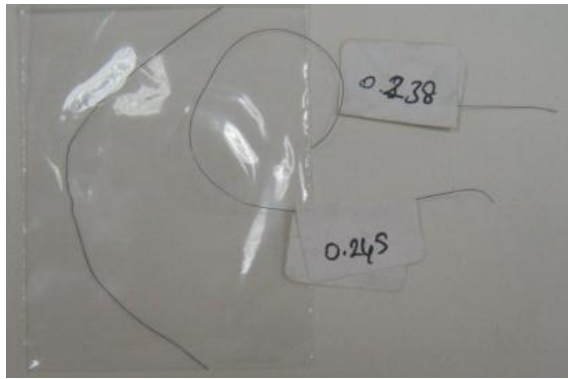
(a)

(b)
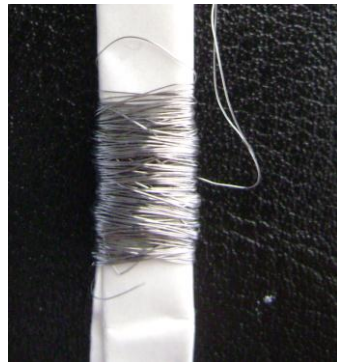
(c)

(d)

Figure 3.1. Picture of the metal templates (a) Ti wire, (b) Ti plate, (c) Stainless steel wire and (d) Copper wire.

Table 3.1. Properties of alumina powders as published by their producers
(Source: Baikowski, January 2011; Alcoa,Inc., 2010;
Sumitomo Chemical, Co. Ltd., 2010).

	CT3000SG	AKP-50	CR6	CR15	CR30F
Crystal Form	α	α	α	90%α −10%γ	80%α −20%γ
Purity (%)	> 99.99	> 99.99	> 99.99	> 99.99	> 99.99
Particle Size (μm)	0.5 – 2.0	0.1 - 0.3	0.3 - 0.4	0.2 - 0.3	0.2 - 0.3
Bulk Density (g/cm^3)	1.2	0.6 - 1.1	0.6 - 1.1	0.45	0.3
BET Surface Area (m^2/g)	7.8	9 - 15	6	15	26
Impurity Level Si (ppm) Na (ppm) Mg (ppm) Cu (ppm) Fe (ppm)	≤ 15 ≤ 3 ≤ 4 ≤ 1 ≤ 15	≤ 25 ≤ 10 ≤ 10 ≤ 10 ≤ 20	≤ 13 ≤ 13 ≤ 1 ≤ 1 ≤ 4	≤ 13 ≤ 13 ≤ 1 ≤ 1 ≤ 4	≤ 16 ≤ 13 ≤ 1 ≤ 1 ≤ 5

3.2. Experimental Method

The flowchart of the experimental work followed in this thesis is given in Figure 3.2. Powder samples were pressed with Ti wire before being fried at high temperature.
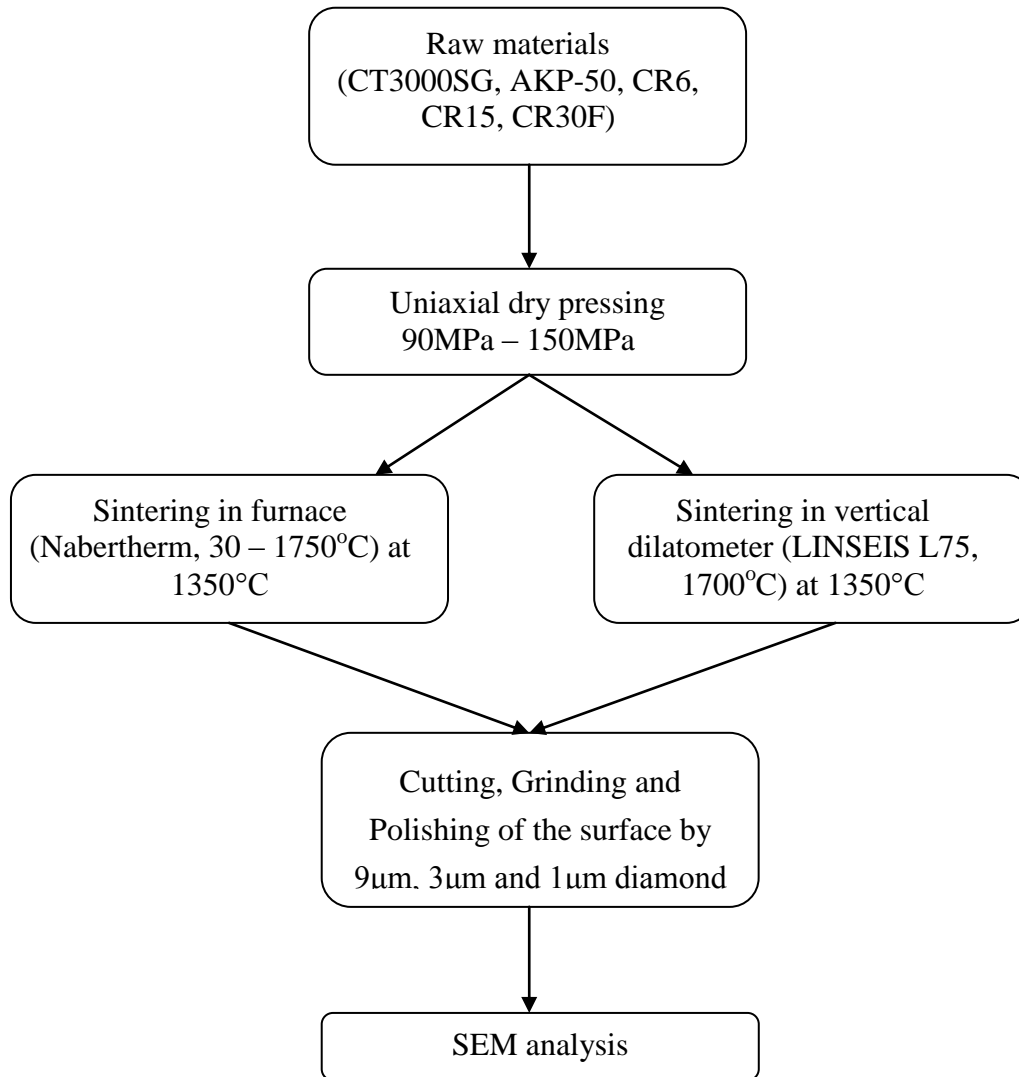
Figure 3.2. Flowchart of the experimental work followed in this thesis.

3.2.1. Co-Pressing with Single-action Mode of Uniaxial Pressing

The alumina pellets were prepared by single-action mode of uniaxial pressing (UP) at two different pressures: 90MPa and 150MPa (Yıldız Hydraulic Press). The co-pressing method is shown in Figure 3.3. This procedure was used in single-action-mode of UP. The alumina powder was poured into die cavity (Φ= 15mm) and was placed down at its bottom by touching with a metal rod. The metal wire (8mm long) was placed on this alumina powder on top of which more alumina powder was poured and the whole pellet was co-pressed at desired pressure.
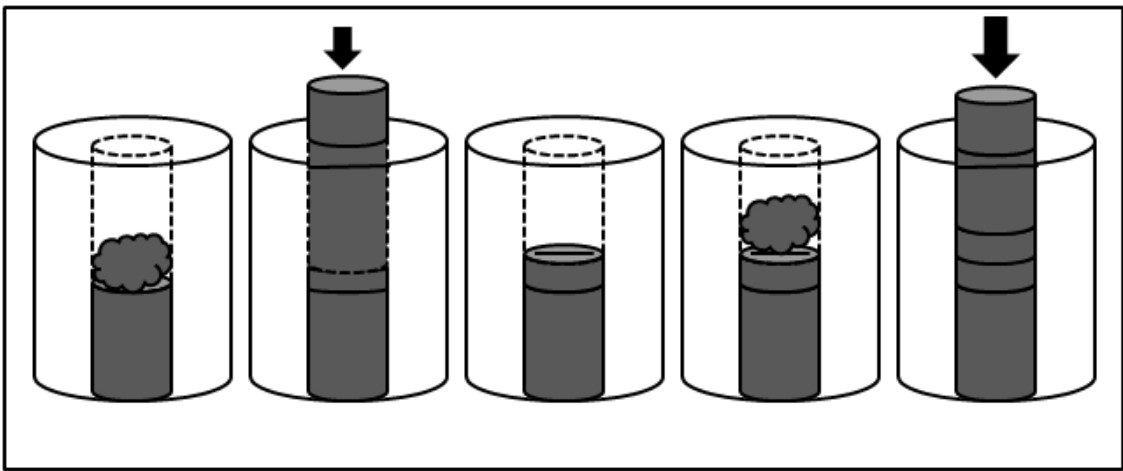
Figure 3.3. Schematic illustration of uniaxial single action co-pressing method.

3.2.2. Sintering Samples and Preparation for Analysis

The samples were sintered at 1350°C for 4 hours in air in the box kiln (Nabertherm, 30 – 1750°C). Heating rate was 5°C/min and cooling rate was 10°C/min. Archimedes method was used to measure densities of all samples. Then, all of the samples were cut with diamond disc, and the surfaces of all sintered samples were machined to produce a straight ground and polished surface. 1200, 800, 600, 320, 180 grit grinding paper (Presi, Megaprex, France) and 9 μm, 3 μm and 1 μm diamond suspensions were used for grinding and polishing to obtain uniform surface (Buehler, Metadi). Finally, samples around 13mm of diameter and 7mm of thickness, were obtained. These samples were then ready for SEM analysis.

3.2.3. Preparation of the Samples for Sintering in Dilatometer

Samples were prepared in the same way as samples prepared for the box kiln. The samples were sintered at 1350°C for 4 hours under air atmosphere in vertical dilatometer (LINSEIS L75, Germany) and the heating rate was 5°C/min, respectively. The samples were cut and the surfaces of all densified samples were ground and polished. 9 µm, 3 µm and 1 µm diamond suspensions were used for polishing (Presi, Mecapol 200) and samples 6mm of diameter and 4 mm of thickness were produced. SEM results of these samples were analyzed. Figure 3.4 shows pressed samples before and after sintering.
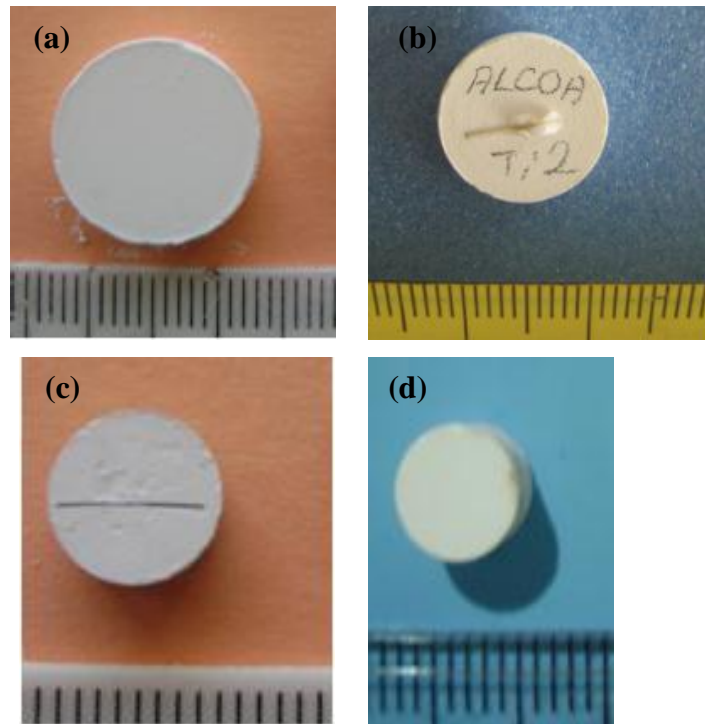
Figure 3.4. Pressed samples: (a) before sintering for furnace, (b) after sintering in the furnace, (c) before sintering for dilatometer and (d) after sintering with the dilatometer.

3.3. Density Measurements

The final density was measured by the Archimedes method (ASTM C 20-87). The immersion liquid was water. The theoretical density of alumina is 3,98 g/cm^3.

3.4. Characterization

In this section, characterization techniques for investigating the samples were described. The techniques used were scanning electron microscopy (SEM, Phillips XL-30S FEG and FEI Quanta250 FEG) for microstructural characterization and BET surface area (BET, Micromeritics Gemini V) for measurement of surface area of alumina powders.

3.4.1. Scanning Electron Microscopy (SEM)

Scanning electron microscope (SEM, Phillips XL-30S FEG and FEI Quanta250 FEG) was used to investigate the surfaces of the alumina samples for interpreting the porous and dense microstructures.

3.4.2. BET Surface Area Measurement

BET surface area measurement (BET, Micromeritics Gemini V) was used to explore the surface area of the alumina powders for measuring the pore volumes and pore sizes.

CHAPTER 4

RESULTS AND DISCUSSION

In this part, densification behaviors, sintering, and microstructures of the samples were investigated by BET surface area, dilatometer (Linseis) and scanning electron microscopy (SEM).

4.1. Densification Behavior of the Powders

Figure 4.1 shows relative shrinkages of alumina (CR6, CR15, CR30F, CT3000SG and AKP50) samples at a heating rate of $5^{o}C$/min. Figure 4.2 shows temperature versus time schedules of sintering tests.
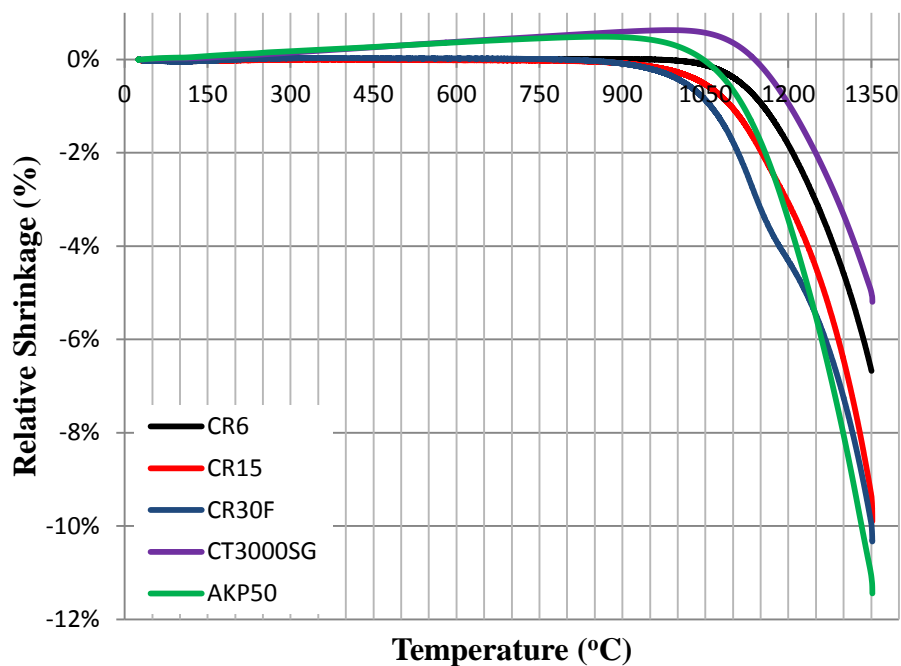

Figure 4.1. Relative shrinkage curves for powder compacts (UP150 MPa) of alümina CR6, CR15, CR30F, CT3000SG and AKP50 during sintering at a heating rate of $5^{o}C$/min.

Figures 4.3 and 4.4 show relative density and densification rates of alumina CR6, CR15, CR30F, CT3000SG and AKP50 samples at a heating rate of 5°C/min. They were sintered with a heating rate of 5°C/min for soaking time of 4 hour at 1350°C. In this case, alumina CR6 was found to have a final density of 94%, while alumina CR15 and CR30F had a density of 93%. Alumina CR15 and CR30F have different types of alumina phases. CR15 contains %90 alpha and %10 gamma alumina phases and CR30F comprises %80 alpha and %20 gamma alumina phases. Hence the relative and densification rate curves of these two powders are similar to each other. Phase transformation of gamma alumina to the alpha form involves heating between 1100 and 1200°C (Figure 4.4). Apart from these, the curves of alumina CR6 and CT3000SG are parallel to each other and the density of CR6 is higher than that of CT3000SG in 800°C and 1350°C. It is observed that the relative density of CT3000SG is 75% at 1350°C. The behavior of relative density of alumina CT3000SG is similar to alumina CR6. On the other hand, the densification rate of alumina AKP50 is higher than that of the other alumina powders. The relative density of AKP50 was found 77% at 1350°C.

Figures 4.3 and 4.4 illustrate the effect of various parameters on densification under constant heating rate (5°C/min) up to 1350°C. Dilatometric curves for alumina CR15 and CR30F show two regimes: the first R1 is a densification associated with the phase transformation of γ-Al2O3 to α-Al2O3 at around 1125°C, the second RII is the densification of the α-phase at higher temperatures.

Densification of the samples showed the usual three distinguishable regions as a function of temperature (Figure 4.2). According to the first region, the densification began approximately at 900°C. In the second region, between 900 and 1350°C, densification rate was significant. In the final part, approximately 93% density may occur. Therefore, we focused on intermediate sintering part up to 93% density. According to this situation, two peaks, which belong to alumina CR15 and CR30F, were ascertained on the densification rate curves of these alumina powders as different from general powder densification behavior (Figure 4.4).
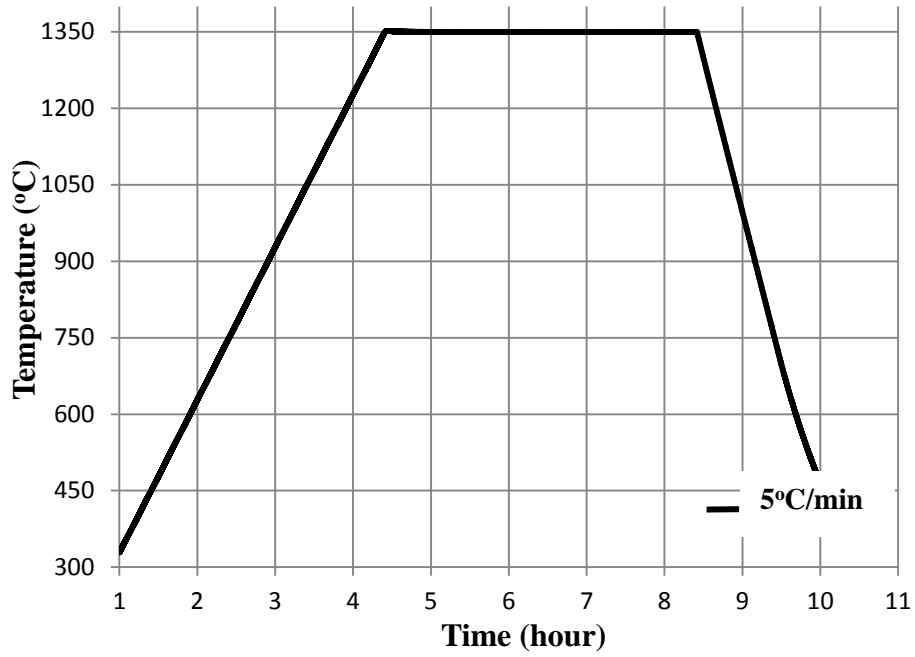
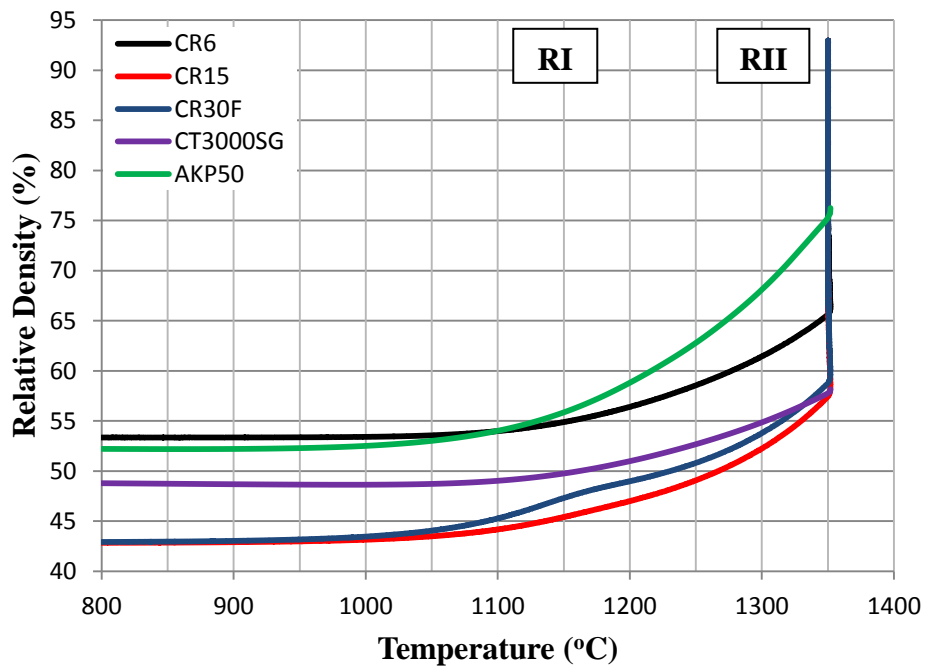Figure 4.2. Temperature versus time schedules of sintering tests.

Figure 4.3. Relative density curve for powder compacts (UP 150MPa) of alumina CR6, CR15, CR30F, CT3000SG and AKP50 during sintering at a heating rate of 5°C/min.

Figure 4.4. Densification rate curve for powder compacts (UP 150MPa) of alumina CR6, CR15 CR30F, CT3000SG and AKP50 during sintering at a heating rate of 5°C/min.

In addition to these curves for different alumina powders, the relative shrinkage, relative density and densification rate of the CR6 alumina powder were investigated at 1500°C for 1min. Figure 4.5 shows relative shrinkage of alumina CR6 samples at a heating rate of 5°C/min at 1500°C. Figures 4.6 and 4.7 show relative density and densification rate of alumina CR6 sample at a heating rate of 5°C/min.

According to the results of tests of 1350°C, the density of all alumina powders have been increased in the 4 hours soaking time. However, the result of test for 1500°C, it is noticed that the density is increased parabolically and the densification rate of CR6 is higher than the test conducted at 1350°C.
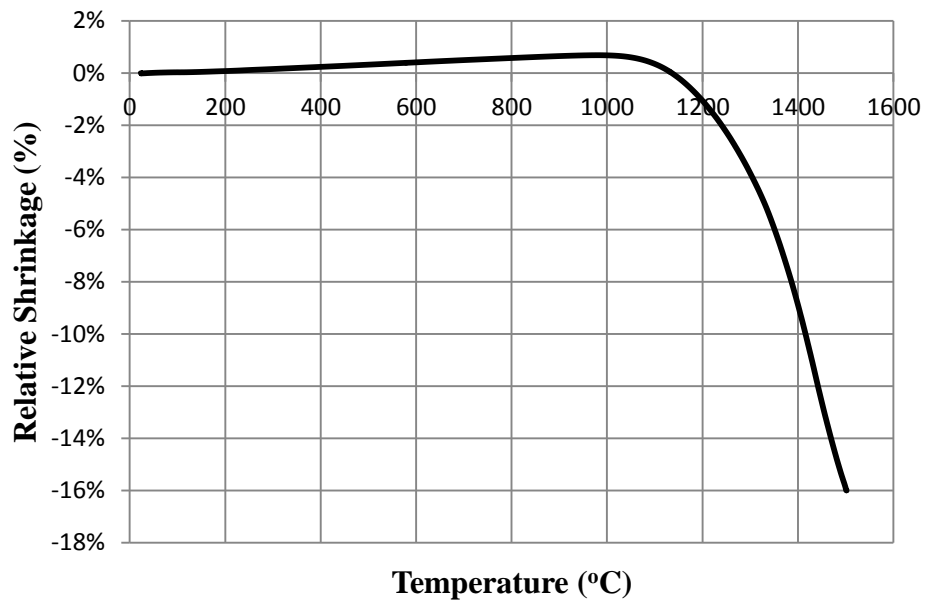
Figure 4.5. Relative shrinkage curves for powder compact (UP150 MPa) of alumina
CR6 during sintering at a heating rate of 5°C/min at 1500°C.
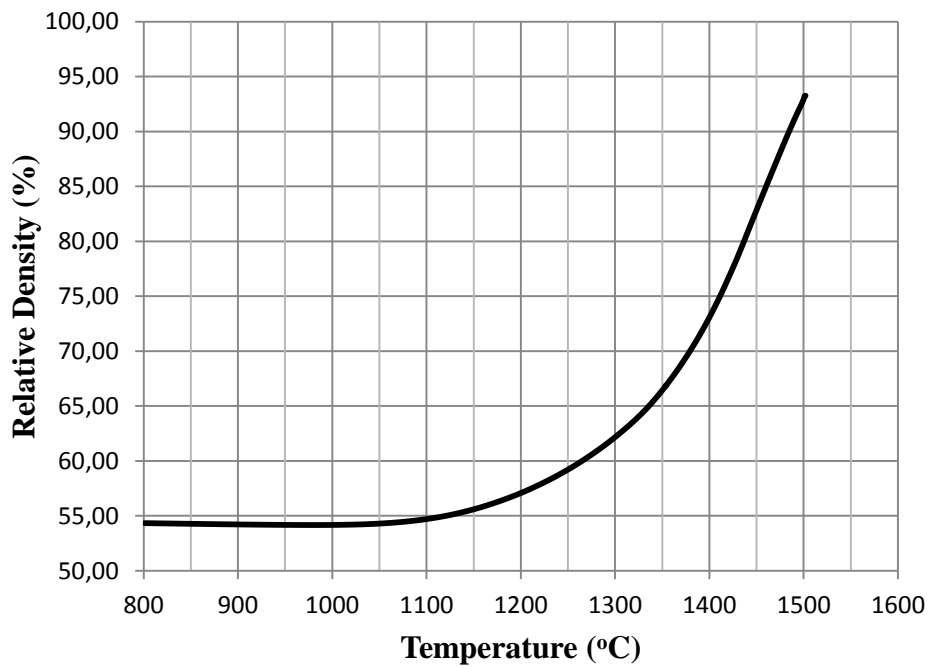
Figure 4.6. Relative density curve for powder compact (UP 150MPa) of alumina CR6
during sintering at a heating rate of 5°C/min at 1500°C.
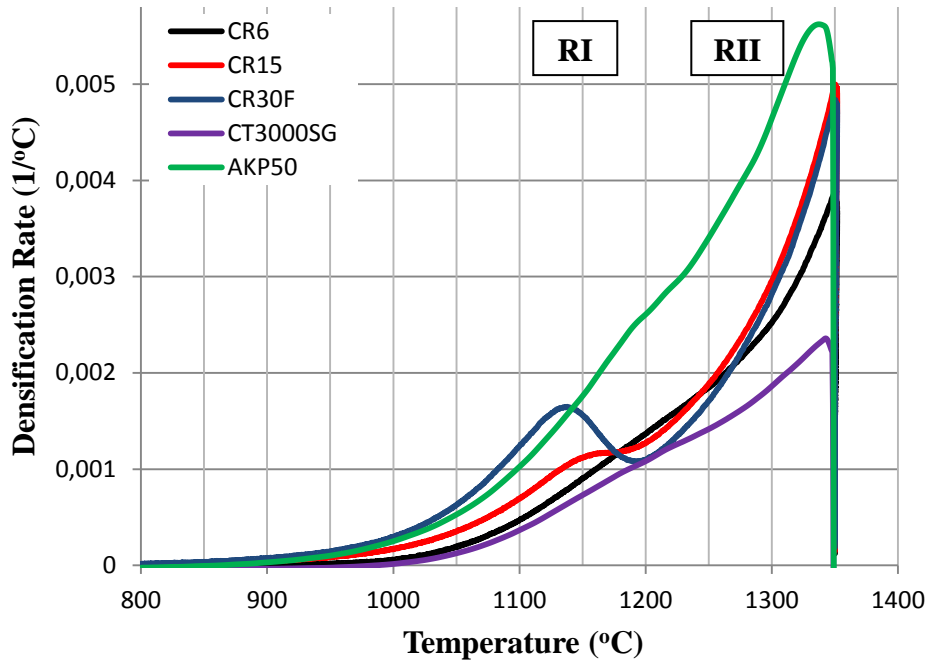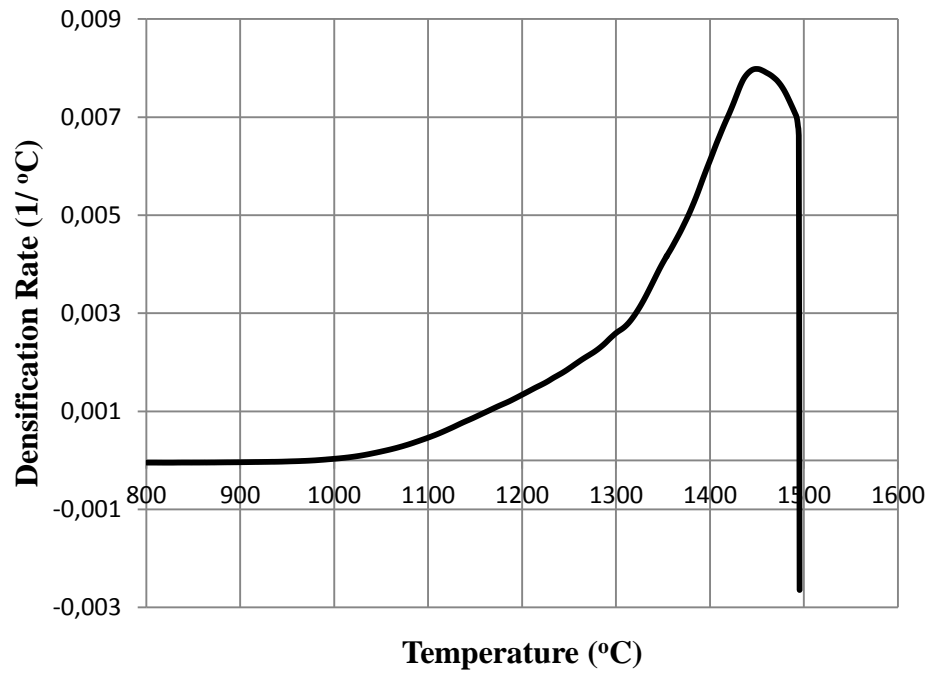
Figure 4.7. Densification rate curve for powder compact (UP 150MPa) of alumina CR6 during sintering at a heating rate of 5°C/min at 1500°C.

4.2. BET Analyses of the Powders

The surface area of alumina powders were measured by BET analysis. Table 4.1 shows the report of the surface area of alumina CR6, CR15 and CR30F. According to this report, it is clear that the particles of alumina CR6 have less surface area, pore volume and pore size than the others, and it is understood that it is not easy for CR6 to create a reaction to the diffusion with the metal templates. All measurements done in this study were lower than those published by the producers.

Table 4.1. BET surface area report.

	CT3000SG	AKP50	CR6	CR15	CR30F
Surface Area					
Specific Surface Area (m²/g)	6.46	10.26	4.02	12.16	21.60
External Surface Area (m²/g)	4.70	8.82	1.87	8.57	17.06

4.3. Scanning Electron Microscopy (SEM)

4.3.1. Alumina

The electron microscopy images of alumina powders are shown in Figure 4.8. The alumina CR6, CR15, CR30F powders were in a softly agglomerated form all with submicron particle sizes as seen in the SEM images. The particle size of alumina CT3000SG was finer than 300nm while alumina AKP50 had a particle size of approximately 200nm and less.
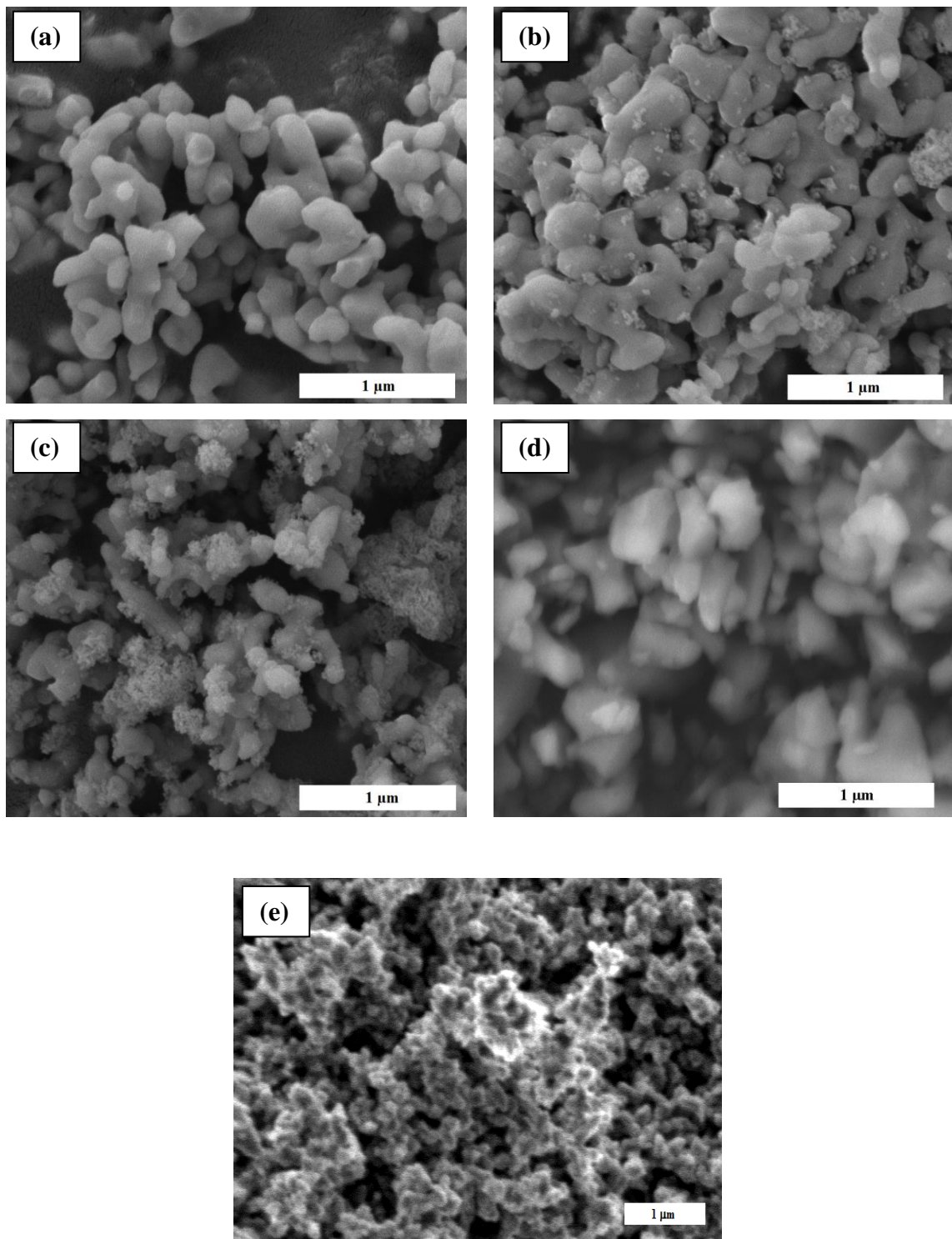
Figure 4.8. SEM images of alumina powders (a) alumina CR6 (b) alumina CR15
(c) alumina CR30F (d) alumina CT3000SG (e) alumina AKP50.

4.3.2. Metal Templates

The electron microscopy images of metal templates are shown in Figure 4.9. It is clear that the diameter of titanium wire and plate are roughly 125µm, while the diameter of copper and stainless steel wire are lower than 100µm.
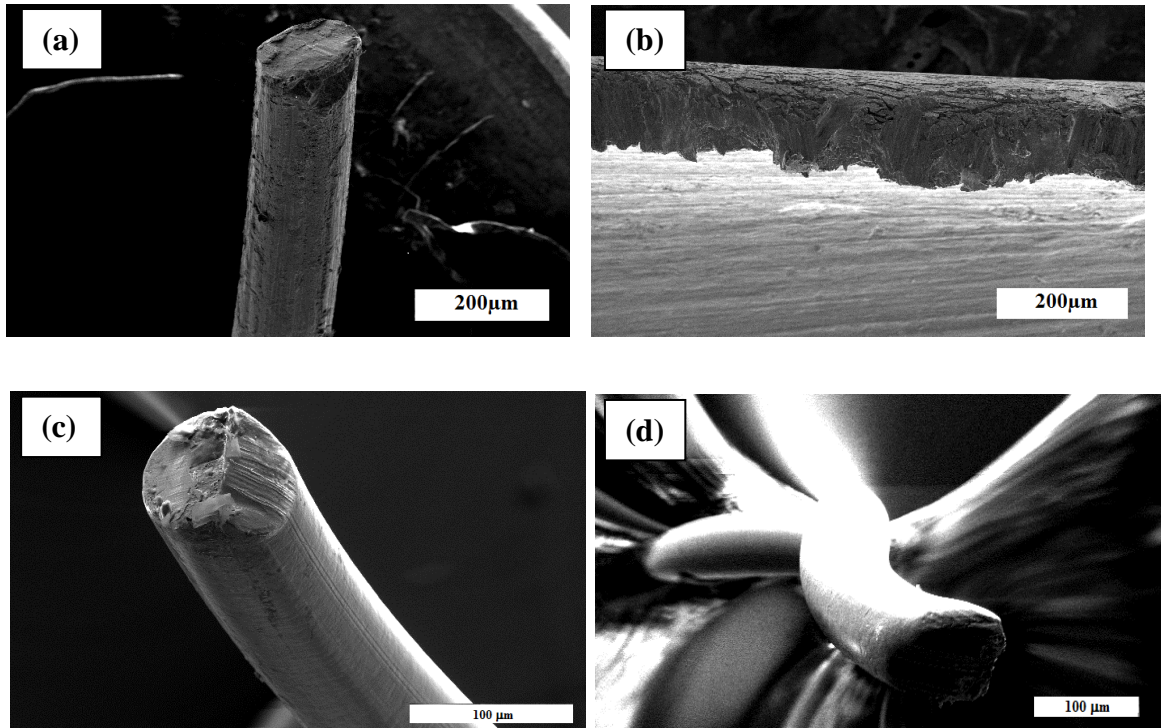
Figure 4.9. SEM micrographs of metal templates (a) Ti wire (b) Ti plate (c) Copper wire (d) Stainless steel wire.

EDS analysis results helped us identify the composition of the metal templates (Figures 4.10-13, Table 4.2.).

According to EDS analysis of titanium wire and plate, these metal templates are rich in titanium. On the other hand, these metal templates are attached with carbon tape, which should not be overlooked while examining the analysis.

It is understood that copper wire and stainless steel wire are rich in copper and steel.
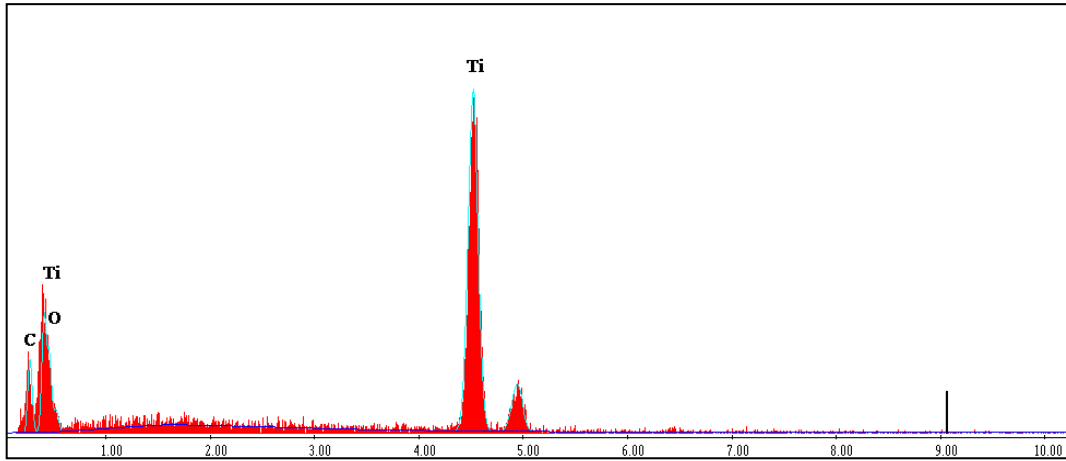
Figure 4.10. EDS analysis of the Ti wire.
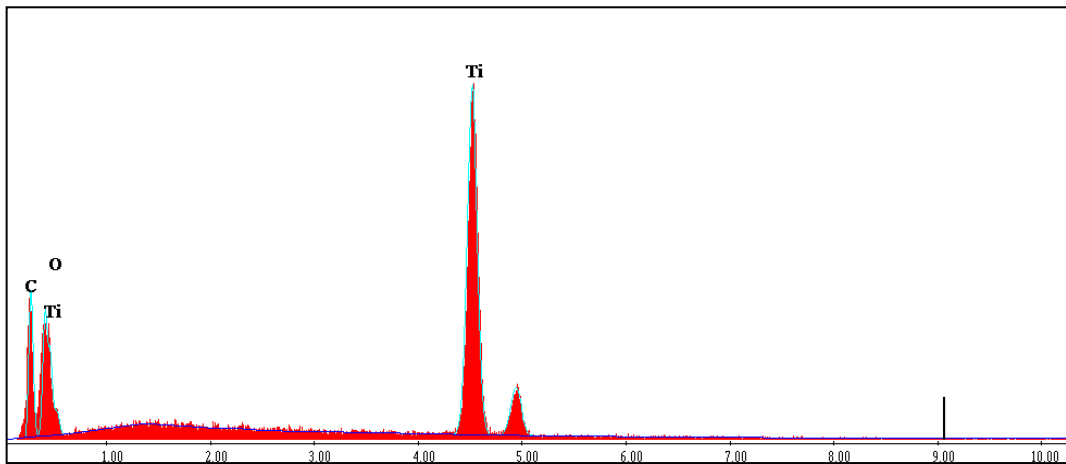
Figure 4.11. EDS analysis of the Ti plate
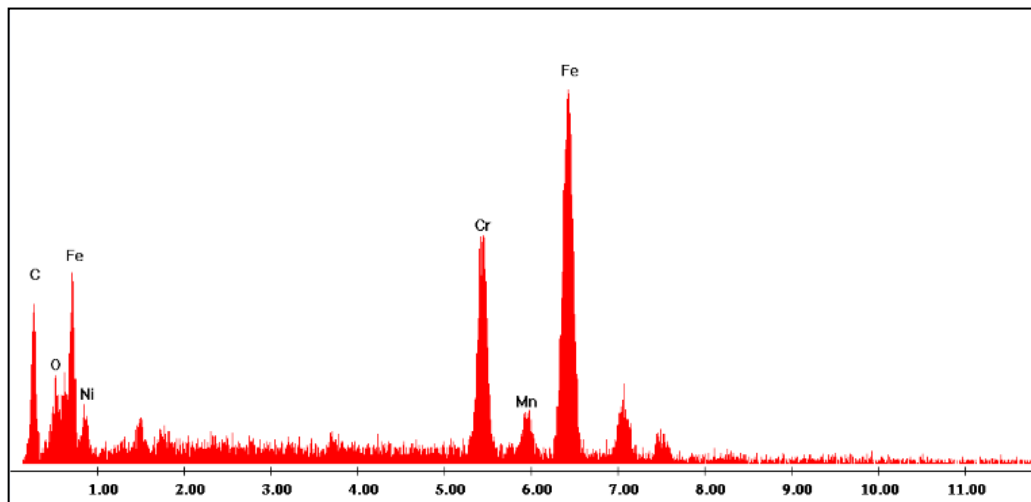
Figure 4.12. EDS analysis of the stainless steel wire
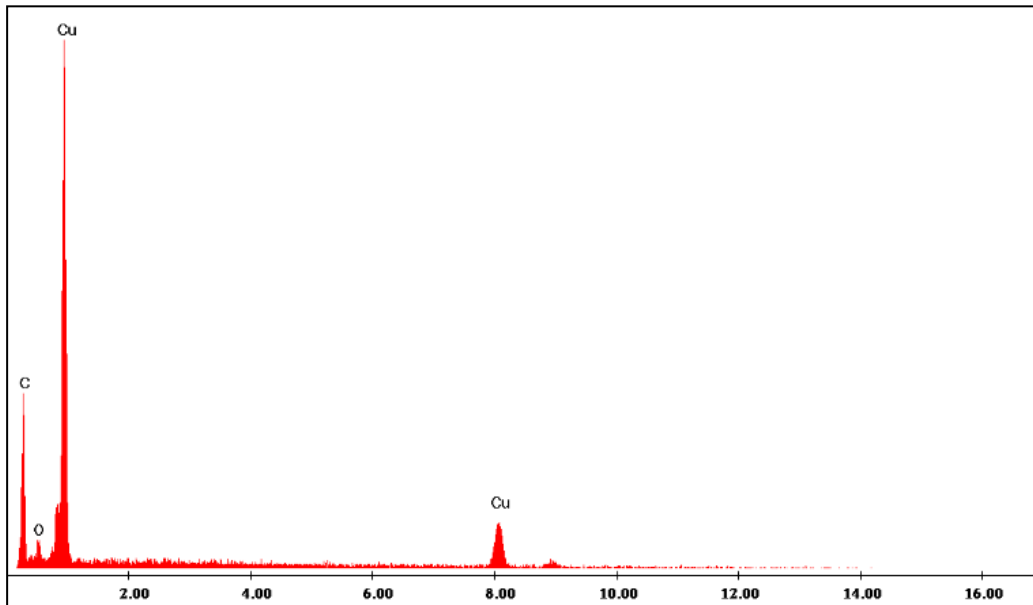
Figure 4.13. EDS analysis of the copper wire

Table 4.2. EDS analysis results of chemical compositions of metal templates.

	Ti (wt%)	Ni (wt%)	Cu (wt%)	Cr (wt%)	Fe (wt%)
Ti Wire	87,9	-	-	-	-
Ti Plate	82,2	-	-	-	-
Stainless steel Wire	-	5,9	-	19,4	57,6
Copper Wire	-	-	88,4	-	-

4.3.3. Ti Diffusion into Alumina

In this section, titanium diffusion into alumina was investigated. Figure 4.14(a) and (b) show the picture of the sample after sintering for top and cross sectional view.

(a)   (b)
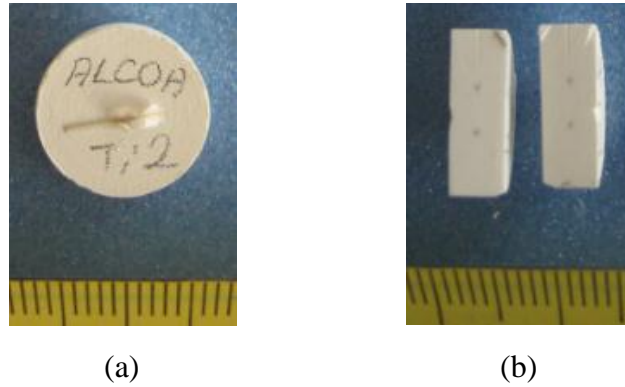
Figure 4.14. Picture of the sample after sintering. (a) Top view and (b) cross sectional view. Notice the dark spots on the cross section that correspond to the location of Ti wire.

Electron microscope images of pressed alumina powders containing Ti wires sintered at 1350°C are shown in Figure 4.15. There are several similarities between the five images, it is apparent in Figure 4.15.

(i)   Each image shows a wide interdiffusion region around the Ti wire.

(ii)   Each image shows some porosity and void formation aligned with the wire.

The interdiffusion region is fractionally restricted in all five states rather than a solid solution diffusion profile that would be more diffuse. The first justification of this situation is compound formation. Next justification is that the diffusing types have come across a barrier of some forms, perhaps connected to exhaustion or removed from a part of the diffusion mechanism.

The cavity formation is a result of the creation of Kirkendall porosity (Kirkendall, 1947) in which the vacancies are left behind by faster diffusing species that coalesce into pores and in this case larger cavities (Goodshaw et al., 2009).
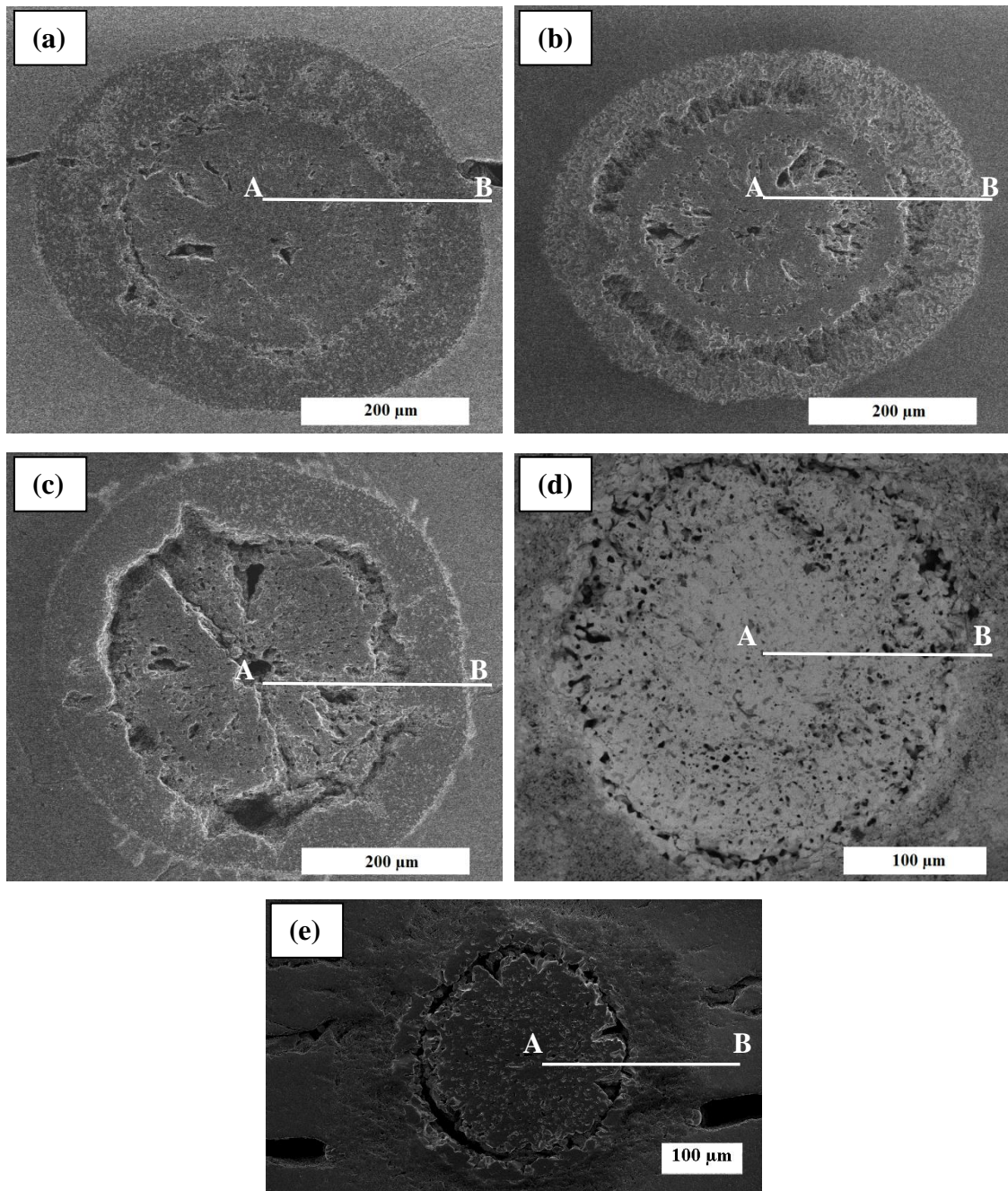
Figure 4.15. SEM micrographs of alumina that used Ti wire (a) alumina CR6 (b) alumina CR15 (c) alumina CR30F (d) alumina AKP50 (e) alumina CT3000SG.

According to Figure 4.15, some of the samples had cracks and porosity in alumina. This is most likely because the sintering temperature used here is insufficient to form a dense ceramic from unmilled and undoped powder (Goodshaw et al., 2009). Secondly, the Ti wire seems to be still present in the alumina. Therefore, the diffusion region in Figure 4.15 shows consequential contrast, and EDS analysis of zones within the diffusion region display that either Al or Ti is present.

Titanium advanced through alumina approximately 100μm at 1350°C in 4 hours of soaking time.

Figure 4.16 shows the phase equilibrium diagram of alumina and titanium oxide. In general, Al_2TiO_5 is obtained by the solid state reaction between Al_2O_3 and TiO_2, which is only thermodynamically possible at temperatures above 1280°C (Low, et al., 2008). Below this temperature, at a range between 900 and 1280°C, metastable Al_2TiO_5 undergoes eutectoid decomposition, forming α-Al_2O_3 and TiO_2 (rutile).
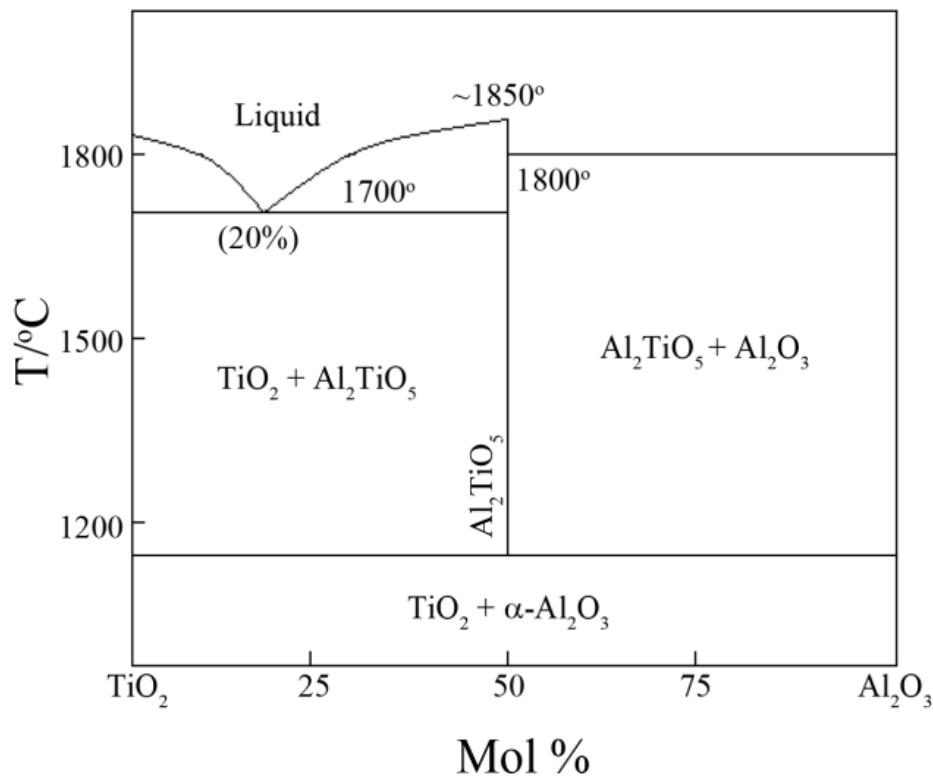
Figure 4.16. Phase equilibrium diagram of $Al_2O_3 – TiO_2$ system
(Source: Goldenberg, 1968).

Figure 4.17 shows the SEM microstructure of cross section of alumina sample, that used Ti wire. It is noticed that Ti^{+4} was diffused into the surrounding alumina, so the phase of Al_2TiO_5 occured in the middle of the diffusion zone. The Kirkendall porosity is observed in the center and around the boundary between the Ti and alumina samples.
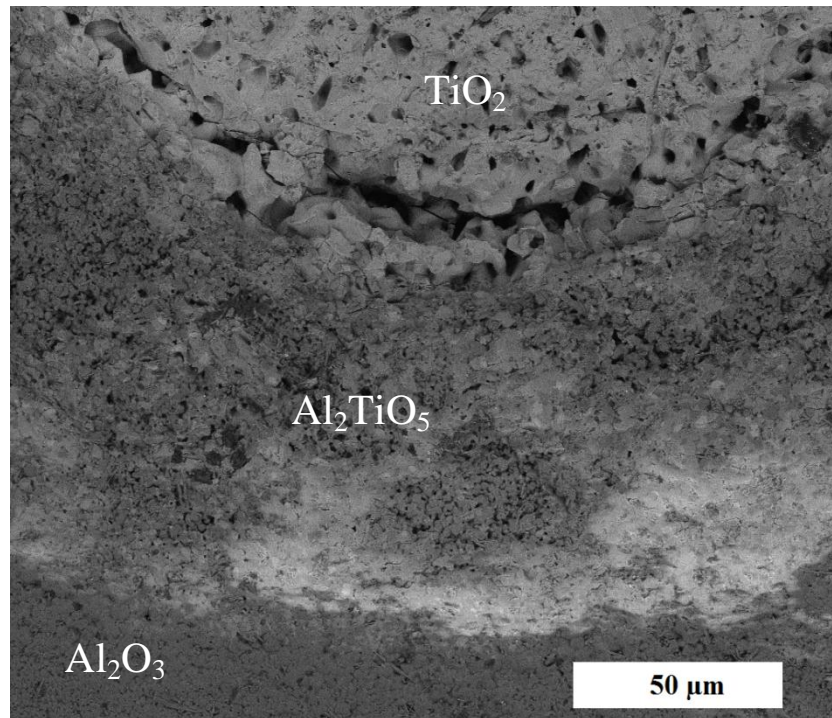
Figure 4.17. SEM micrographs of cross section of alumina (CT3000SG) sample containing Ti wire. Notice the diffusion of Ti^{+4} from top to bottom away from the wire into the bulk of alumina. The amount of porosity increases from bottom to top due to Kirkendal effect. An intermediate phase of Al_2TiO_5 formed in the middle.

Figures 4.18, 19, 20, 21 and 22 displays belong to the EDS line analysis results of the different alumina samples containing Ti wire. As can be seen from Figure 4.15 , EDS line analysis of samples occurred in a flat line from A to B. According to EDS analysis, it is observed that Al is present as Al_2O_3, Ti is present as TiO_2 and the compound formed between the two is Al_2TiO_5 (pseudobrookite structure).

According to EDS analysis of these samples, firstly, the concentration profile of Ti is higher than that of Al. During sintering, due to Ti^{+4} ions diffuses into Al_2O_3 and the concentration profile change in the opposite direction. Secondly, the concentration content of Al is higher than Ti.
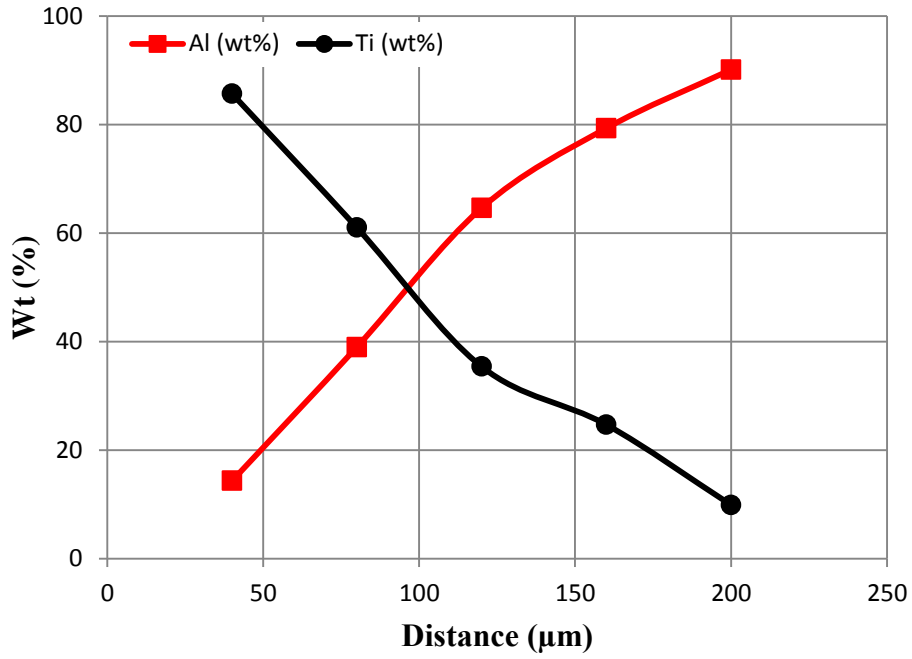
Figure 4.18. EDS line analysis of the sample (CR6).
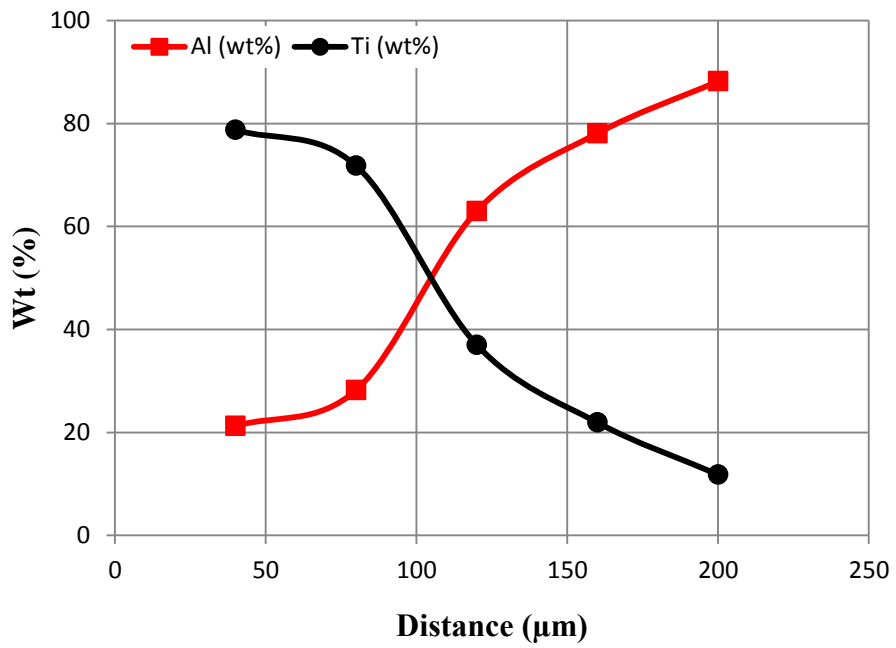
Figure 4.19. EDS line analysis of the sample (CR15).
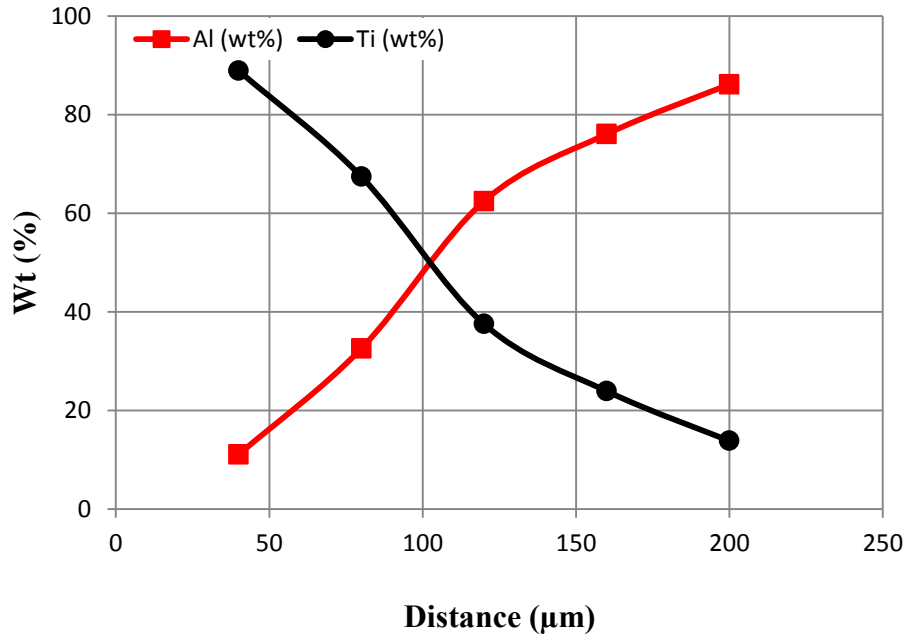
Figure 4.20. EDS line analysis of the sample (CR30F).
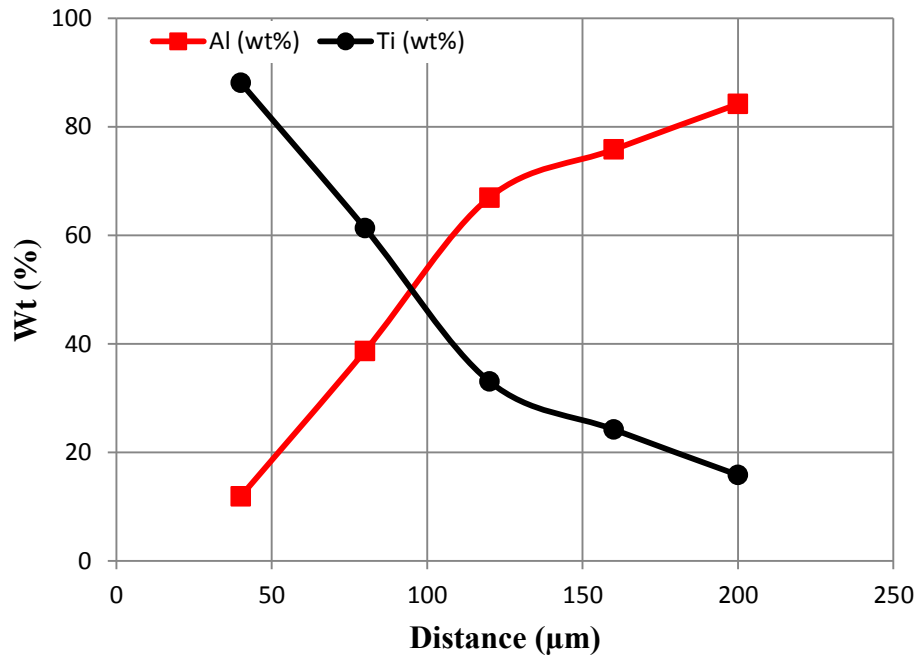
Figure 4.21. EDS line analysis of the sample (AKP50).
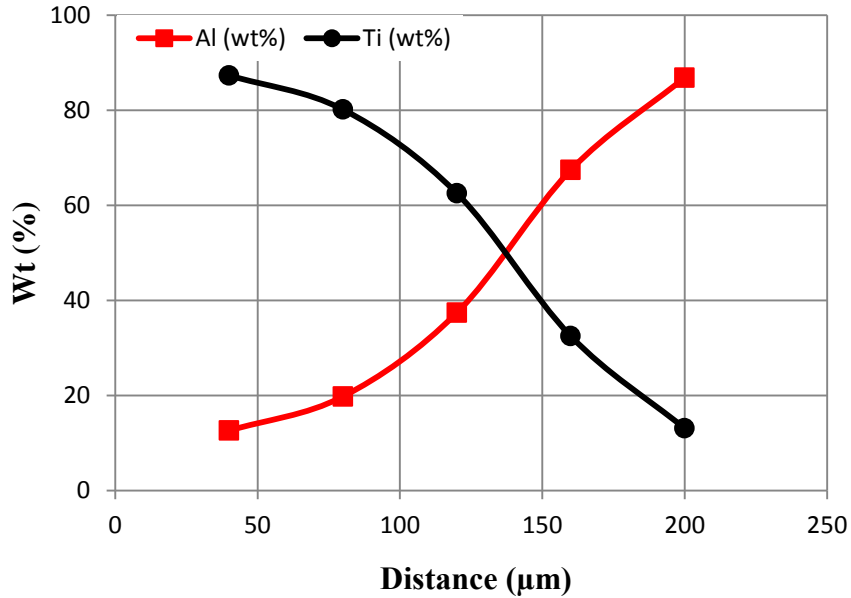
Figure 4.22. EDS line analysis of the sample (CT3000SG).

4.3.4. Sintering Behavior of Titanium Wire Containing Pellets

Figure 4.23 shows the relative shrinkage curves for alumina samples, which titanium wire containing at 1350°C. For the behavior of relative shrinkage, Figures 4.1 and 4.23 are compared and there is no difference. It is clear that the titanium wire does not affect the shrinkage behavior of alumina.
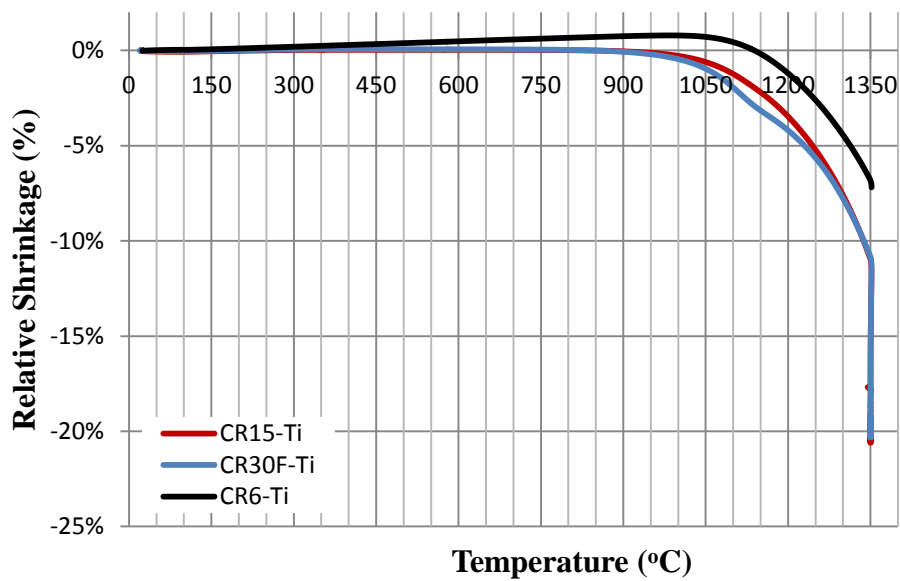
Figure 4.23. Relative shrinkage curves for powder compacts (UP150 MPa) of alumina CR6-Ti, CR15-Ti and CR30F-Ti, that used titanium wire, during sintering at a heating rate of 5°C/min.

Relative density curves of the different alumina samples that contain Ti wire is illustrated in Figure 4.24. It is seen that the densities of the CR6-Ti and the CR15-Ti samples are 78% and 91%, respectively. Figures 4.3 and 4.24 are compared and it is possible to concluded that the density of the samples is higher at 800°C.
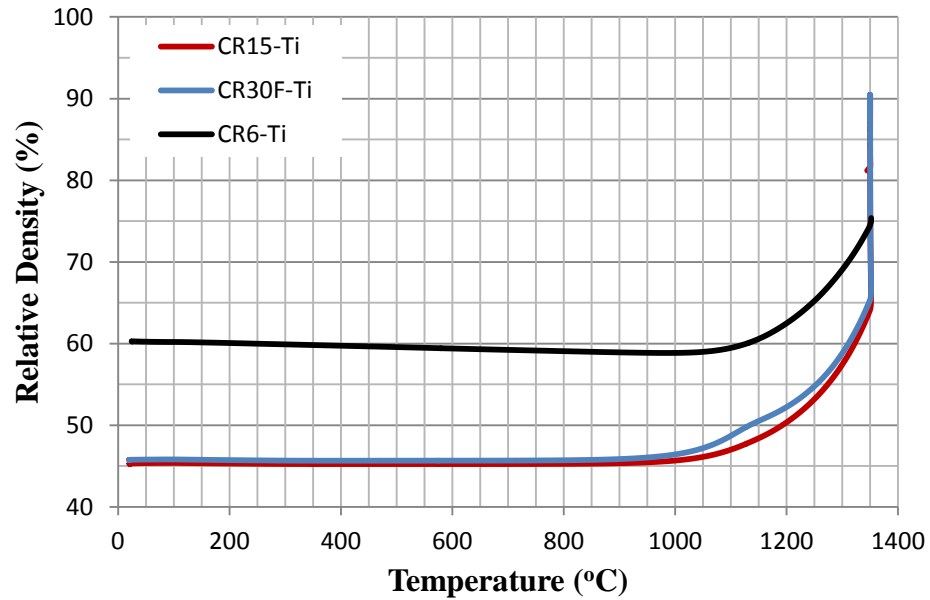
Figure 4.24.   Relative density curve for powder compacts (UP 150MPa) of alumina CR6-Ti, CR15-Ti and CR30F-Ti, that used titanium wire, during sintering at a heating rate of 5°C/min.

In addition to relative density curves of samples containing Ti wire, densification curves of these samples are given in Figure 4.25. If we compare the Figure 4.4 and Figure 4.25, we can see that the diffusion of titanium increases the densification rate of the samples at 1350°C.
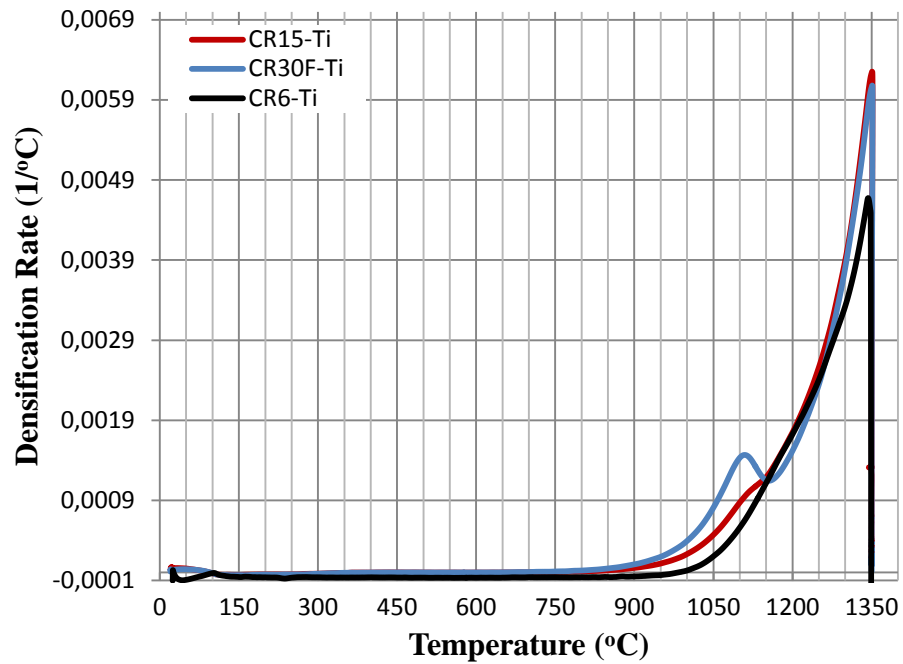
Figure 4.25. Densification rate curve for powder compacts (UP 150MPa) of alumina CR6-Ti, CR15-Ti and CR30F-Ti that used titanium wire, during sintering at a heating rate of 5°C/min.

Figure 4.26 shows SEM micrographs of the CR6, CR15 and CR30F alumina samples that used Ti wire. According to Figure 4.26, all of the samples had porosity in alumina and the CR15 alumina samples have crack. As in Figure 4.15, the titanium wire is still present in the alumina. Titanium proceeded in alumina approximately 100μm at 1350°C in 4 hours of soaking time.
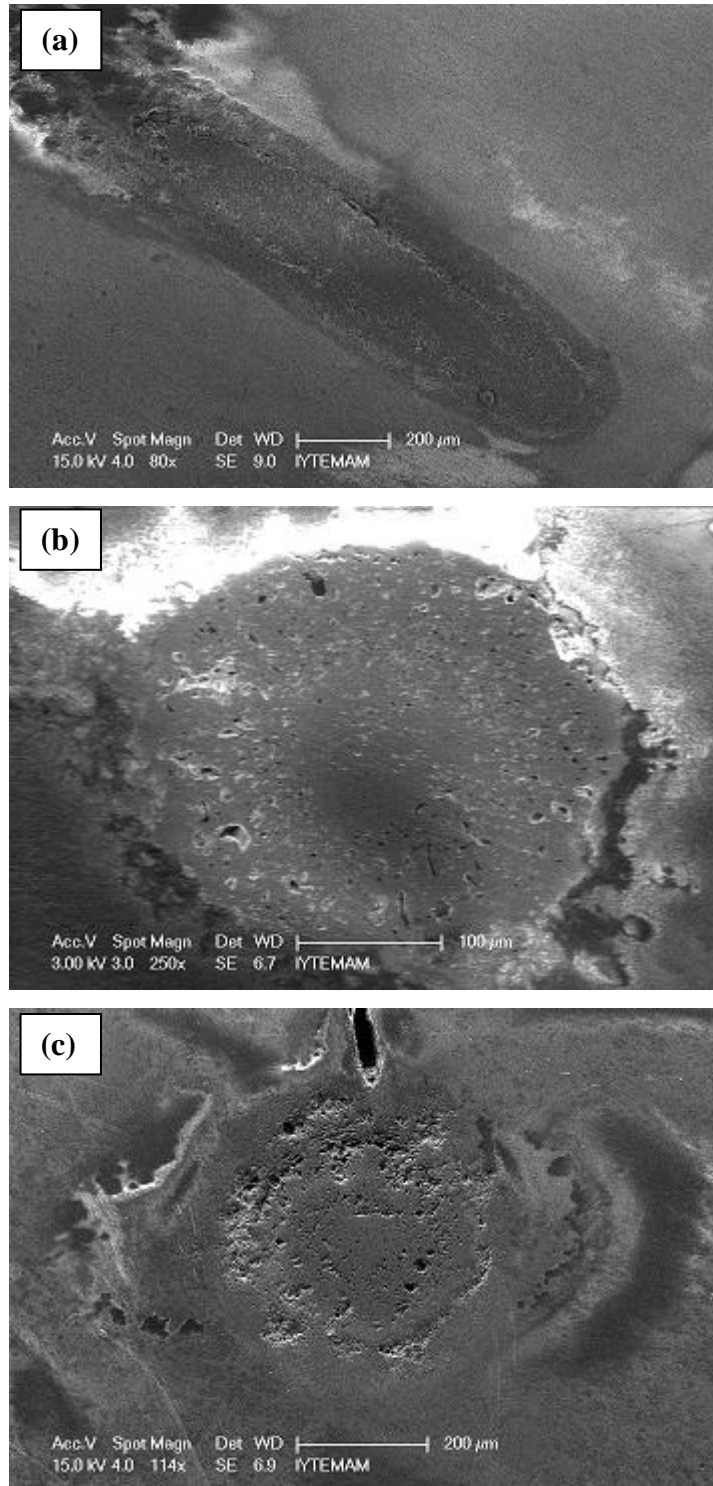
Figure 4.26. SEM micrographs of alumina that used Ti wire (a) alumina CR6-Ti
(b) alumina CR15-Ti (c) alumina CR30F-Ti.

Figure 4.27, 28 and 29 belong to EDS analysis of the CR6-Ti, CR15-Ti and CR30F-Ti alumina samples containing titanium wire. As in Figure 4.18, 19, 20, 21 and 22, during sintering, the concentration profile in the opposite direction varies between Al and Ti.
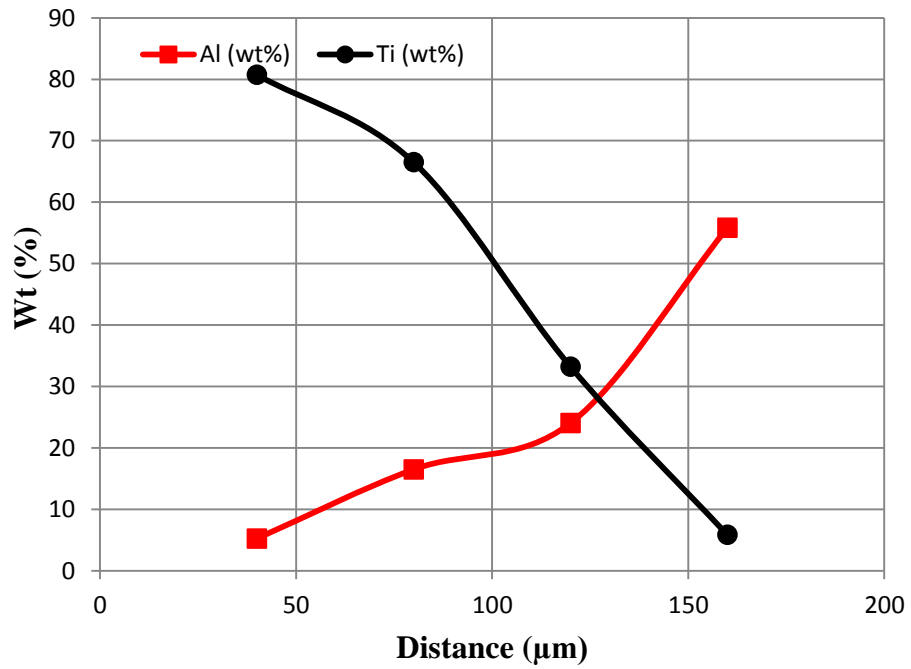
Figure 4.27. EDS line analysis of the sample (CR6-Ti).
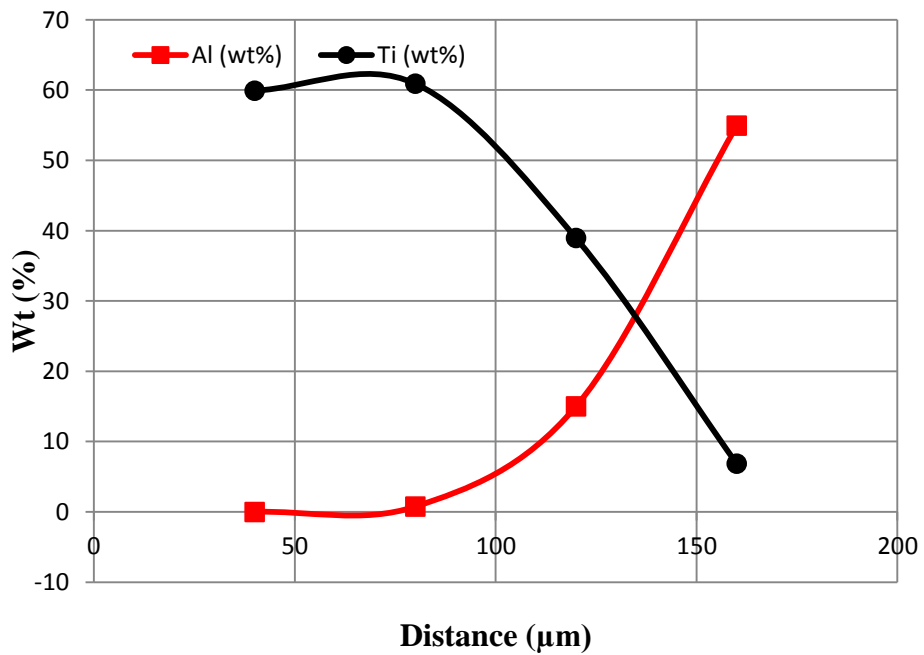
Figure 4.28. EDS line analysis of the sample (CR15-Ti).
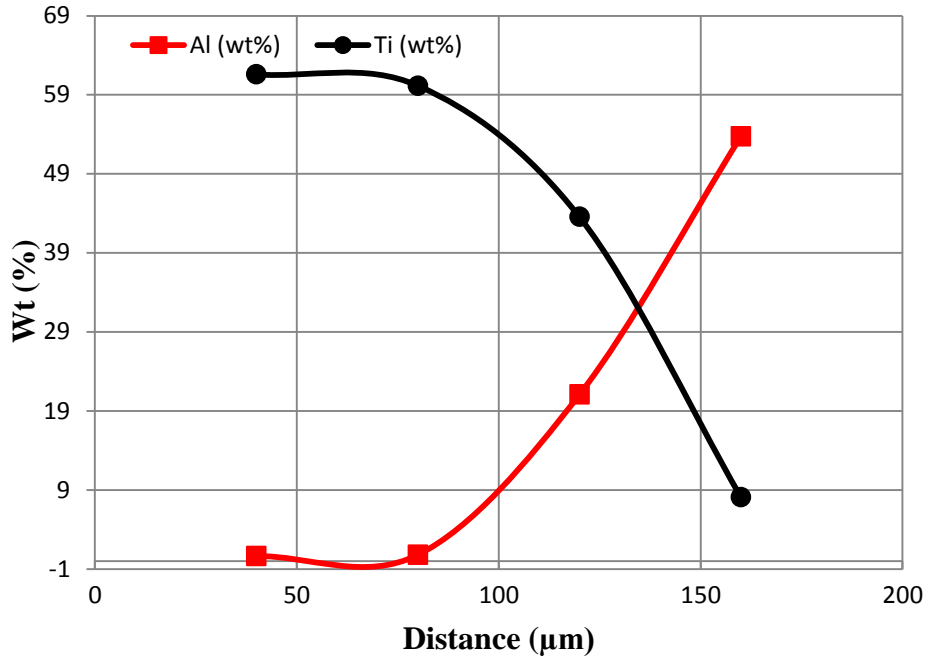
Figure 4.29. EDS line analysis of the sample (CR30F-Ti).

Titanium diffusion in alumina is illustrated in Figure 4.30. It is considered that titanium diffuses into alumina among the grain boundaries, more thoroughly. At the same time, the diffusion of Ti^{+4} happened and also by Kirkendall effect creeping occurred. By slipping among grains, new phases and also micro-pores occurred in the structure of alumina.
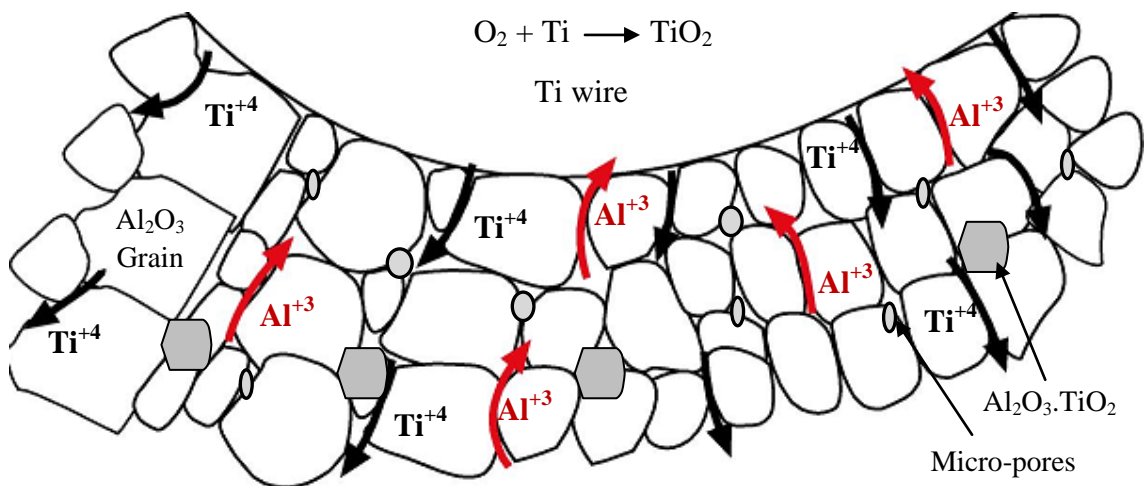
Figure 4.30. Ti diffusion in alumina.

4.3.5. Stainless Steel Diffusion into Alumina

Figure 4.31 shows that the stainless steel wire has almost completely diffused into the surrounding alumina leaving behind a cylindrical void. The control of the void diameter shows that it is larger than the original wire diameter. It is the expected result of sintering densification (Goodshaw et al., 2009).
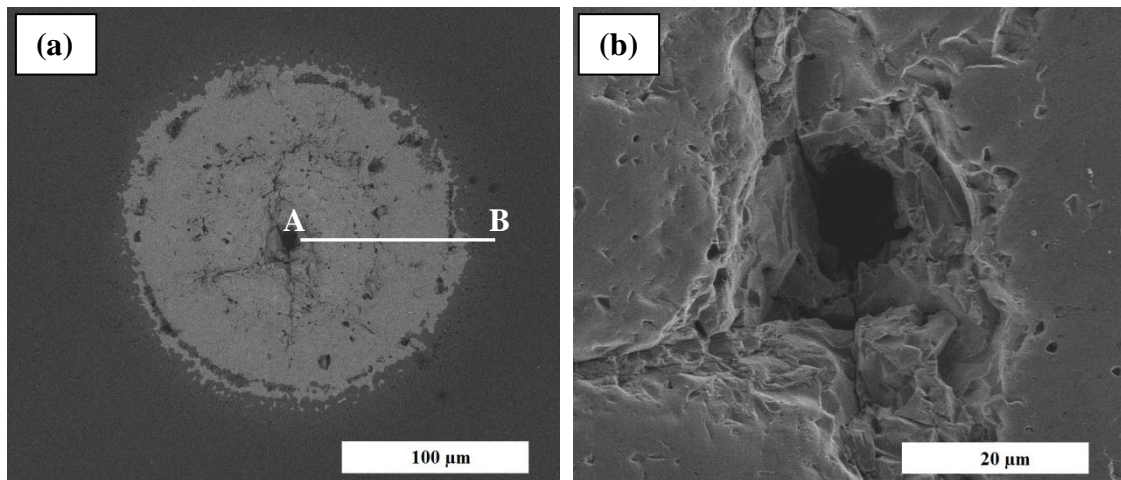
Figure 4.31. SEM micrographs of alumina CR15-St that used stainless steel wire (a) 5°C/min at magnification of 500X (b) 5°C/min at magnification of 5000X.

According to Figure 4.31, it is observed approximately 100µm expansion for stainless steel in alumina for 4 hours as soaking time.

The phase diagram of Fe_2O_3 - Al_2O_3 system is shown in Figure 4.32. According to this diagram, it is clear that $Al_2Fe_2O_6$ (heamatite structure) occured at 1350°C.
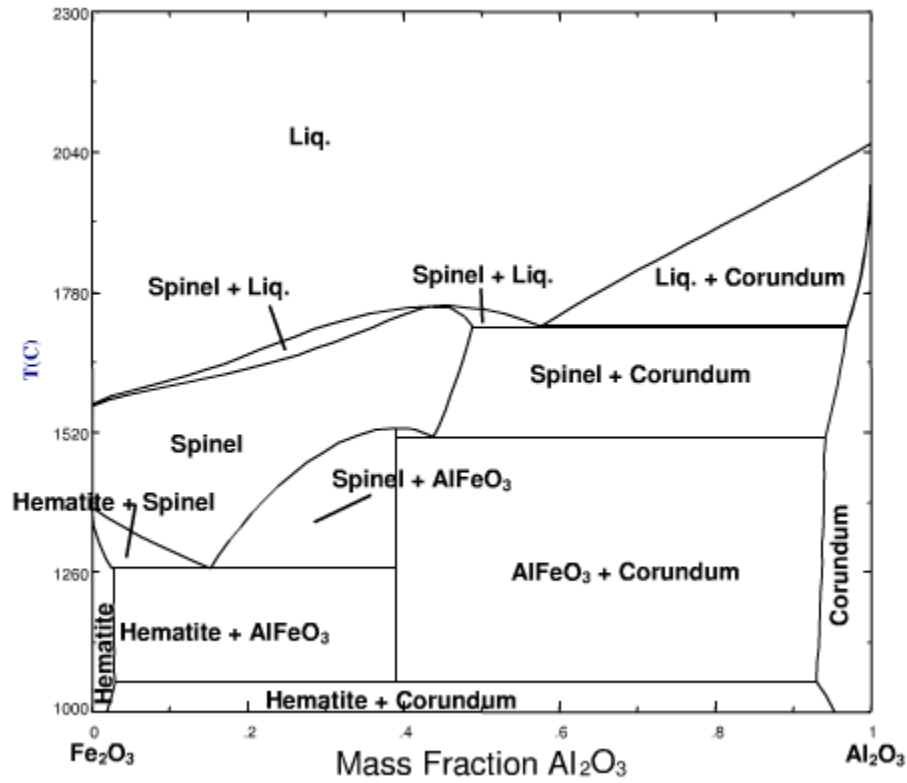
Figure 4.32. Phase equilibrium diagram of Fe_2O_3 - Al_2O_3 system
(Source: Besmannand et al., 2005).

Figure 4.33 shows EDS analysis of the containing stainless steel sample. A and B are shown in Figure 4.31. It is seen that EDS analysis is a flat line from A to B.
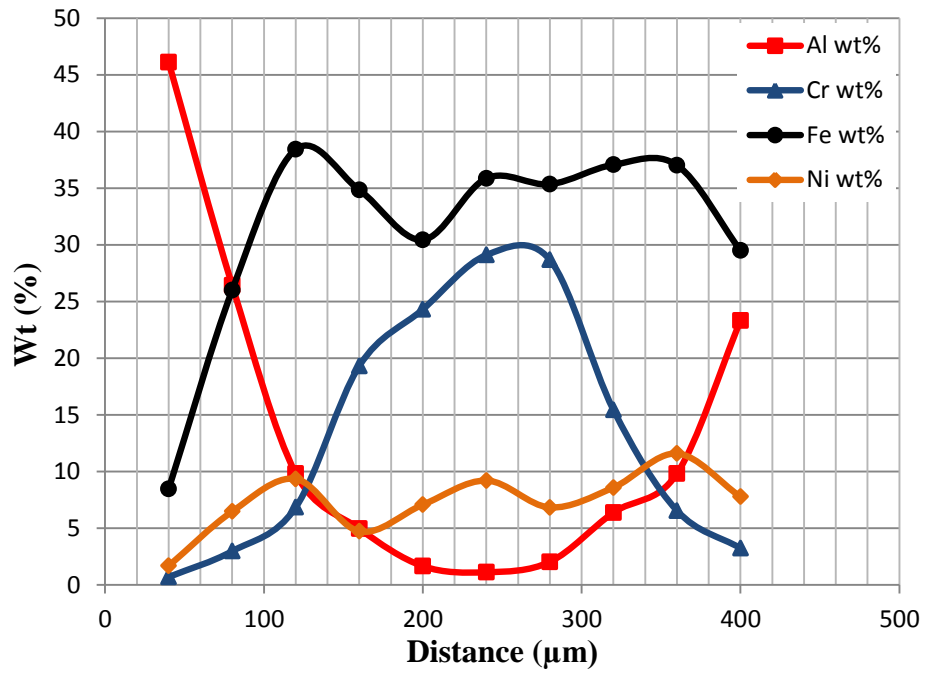
Figure 4.33. EDS line analysis of the sample CR15-St.

4.3.6. Copper Diffusion into Alumina

Copper diffusion into alumina is shown in Figure 4.34. The circle indicates diffusion region. The copper wire has almost completely melted into the alumina leaving behind a void. The void diameter is much larger than the original wire diameter.
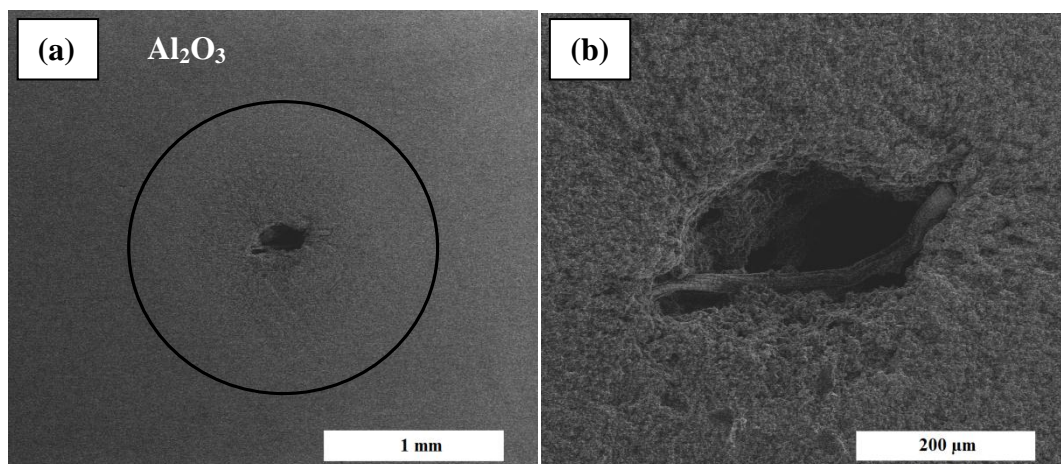
Figure 4.34. SEM micrographs of alumina CR30F that contained copper wire (a) 5°C/min at magnification of 100X (b) 5°C/min at magnification of 500X.

Figure 4.35 shows the phase equilibrium diagram of CuO- Al_2O_3 system. There are several preliminary observations to be made on this diagram. At low temperatures, no Cu_2O is formed, only CuO, which does not react with Al_2O_3. At around 800°C, $Cu(AlO_2)_2= CuAl_2O_4$ begins to be formed in this reported narrow 800-900°C. $CuAlO_2$ is reported to be stable for all temperatures between 900°C and 1260°C, and also in equilibrium with CuO or Al_2O_3 when unbalanced. At 1350°C, copper has been almost completely liquid phase.
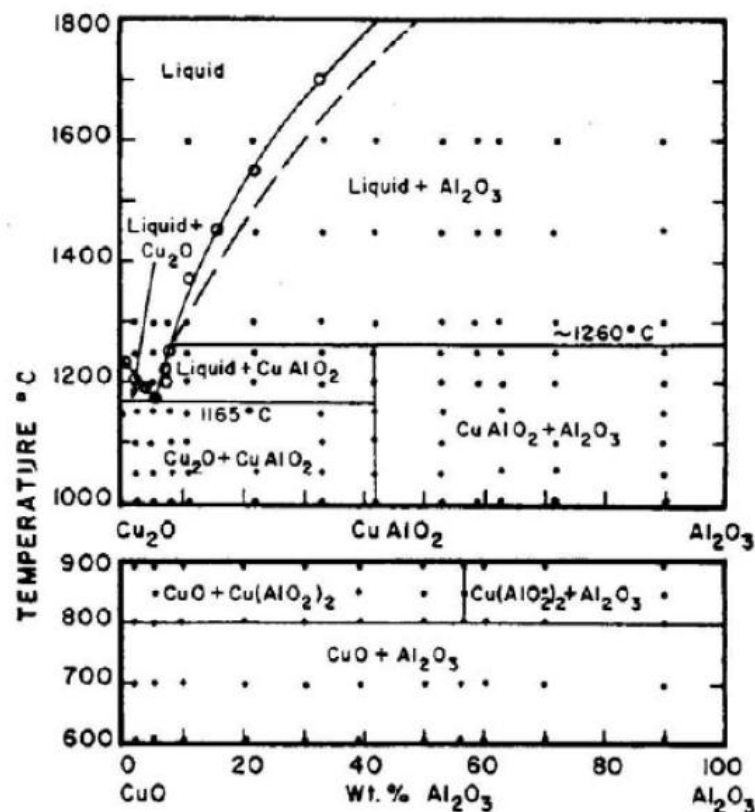
Figure 4.35. Phase equilibrium diagram of CuO - Al_2O_3 system
(Source: Misra et al.,1963).

Figure 4.36 shows EDS analysis of the sample CR30F-Cu. According to EDS results of the sample, Al and O are stable while we cannot see much Cu. Copper is considered to be in liquid phase at 1350°C. It is possible to melt out during heating and only a minor fraction remained in alumina which was sufficient enough to impart some color in the otherwise white alumina ceramic.
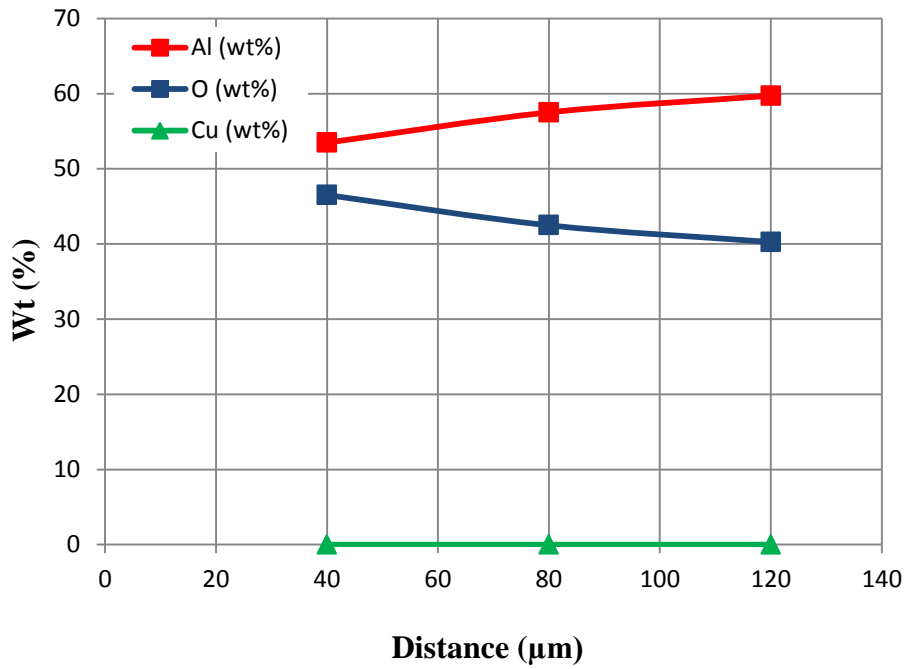
Figure 4.36. EDS line analysis of the sample CR30F-Cu.

Because copper is in the liquid phase at 1350°C, the experiment is repeated at 1000°C. Copper diffusion into alumina at 1000°C is shown in Figure 4.37. Copper wire diffused from exactly the centre of itself into alumina.
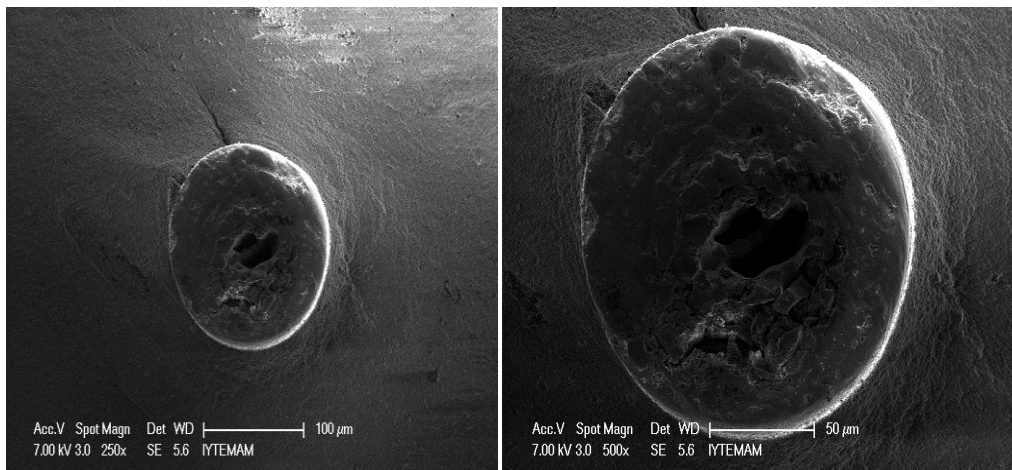
Figure 4.37. SEM micrographs of alumina CR30F that contained copper wire.

Figure 4.38 shows EDS analysis of the sample CR30F. According to EDS results of the sample, the concentration content of Al and Cu changes and copper is diffused into alumina approximately 50µm at 1350°C.
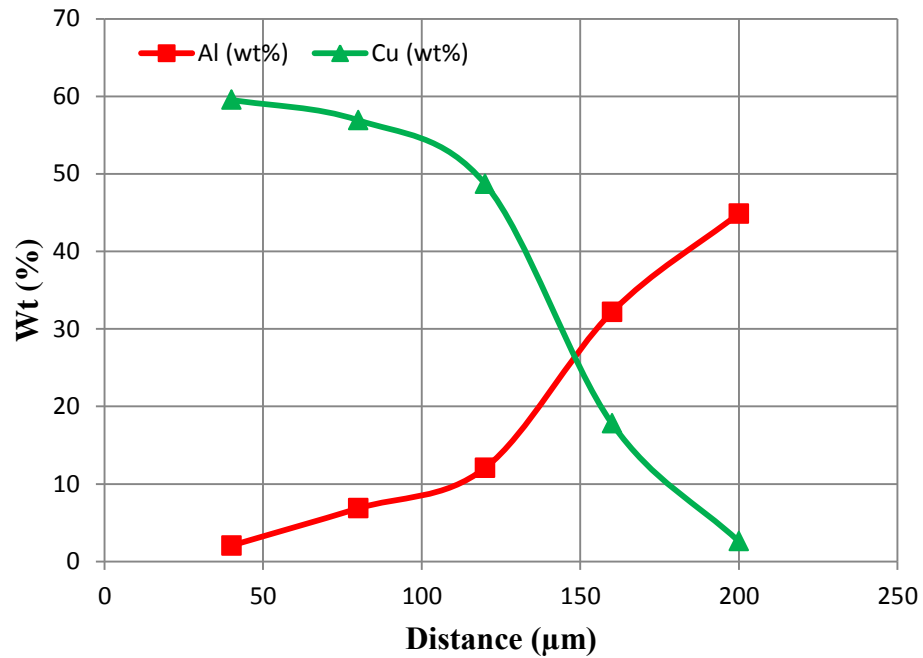
Figure 4.38. EDS line analysis of the sample CR30F.

4.3.7. Results of Sintering of Alumina-Ti plate-Alumina Pellets

Figure 4.39 illustrates the picture of the alumina samples (sandwich structure) after sintering.

(a)   (b)

(c)   (d)
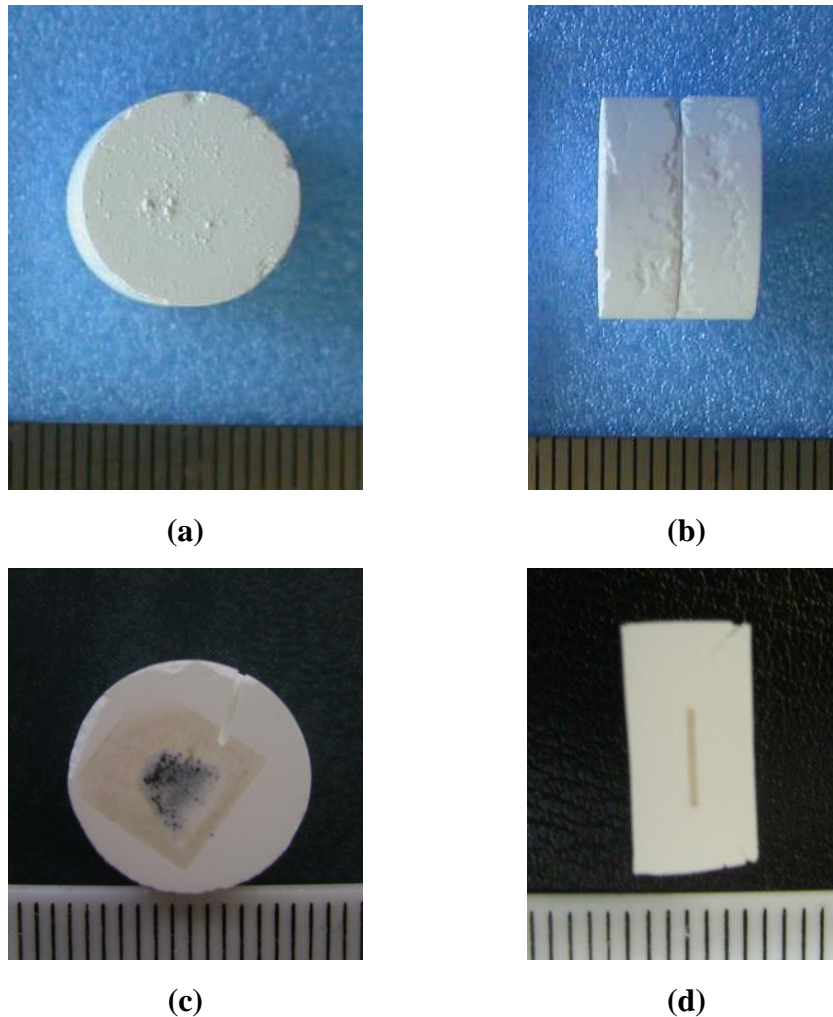
Figure 4.39. Picture of the alumina sample (sandwich structure) (a) and
(b) after sintering (c) fracture surface of sample CR3000SG-
Plt (d) cross sectional surface of sample CR30F-Plt

The SEM micrographs of the alumina sample that contains Ti plate, are given in Figure 4.40. During four hour soaking time, titanium advanced through alumina roughly 130μm at 1350°C. As in the samples, which contains Ti wire, Al_2TiO_5 occurred in the diffusion region, and the alumina samples had porosity. In Figure 4.40 (a), Kirkendall plane and porosity are seen and as a whole they look like craters.
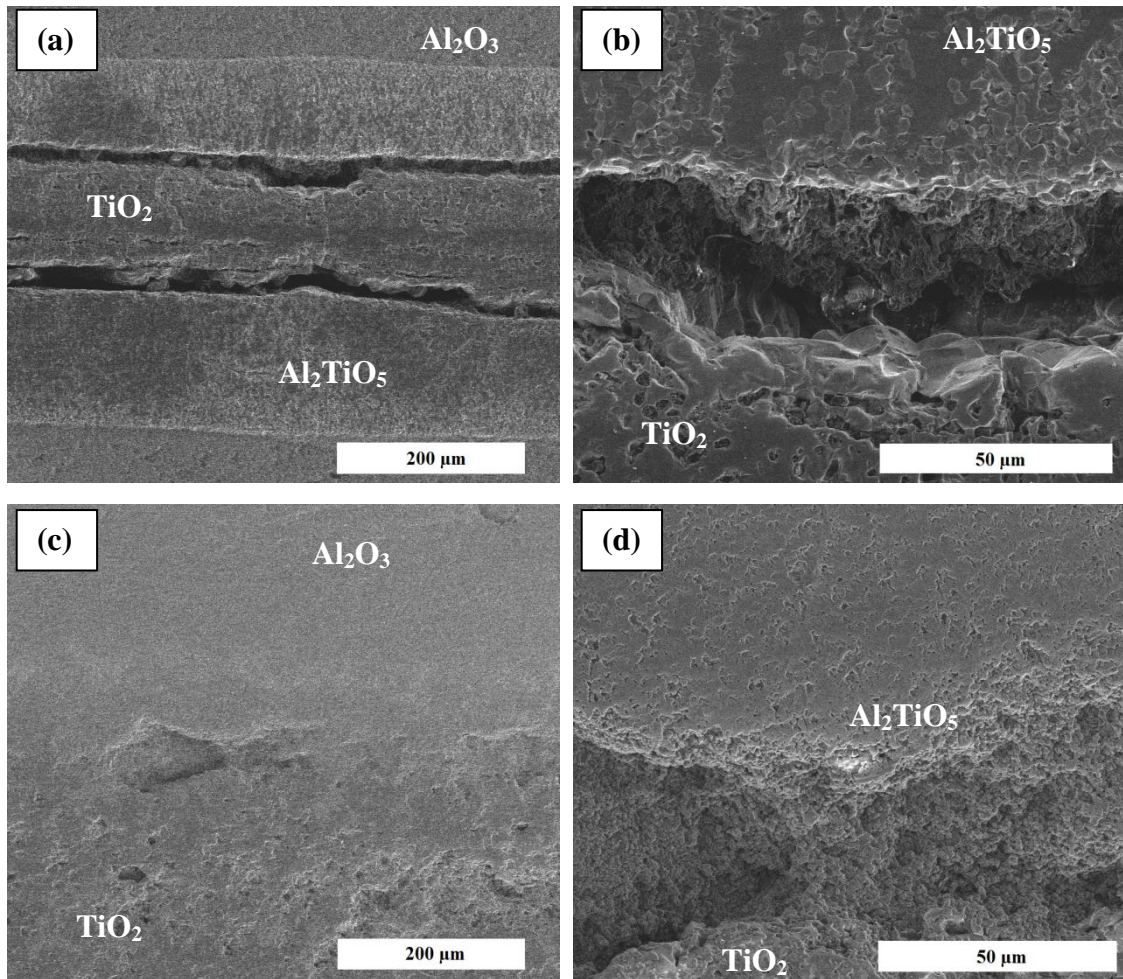
Figure 4.40. SEM micrographs of alumina that used Ti plate (a), (b) alumina CR30F-Plt (c), (d) alumina CT3000SG-Plt.

Figure 4.41 shows the EDS analysis of containing Ti plate alumina sample. In the EDS analysis, it is cleared that during sintering the concentration profile of Ti decreases while Al increases with temperature.
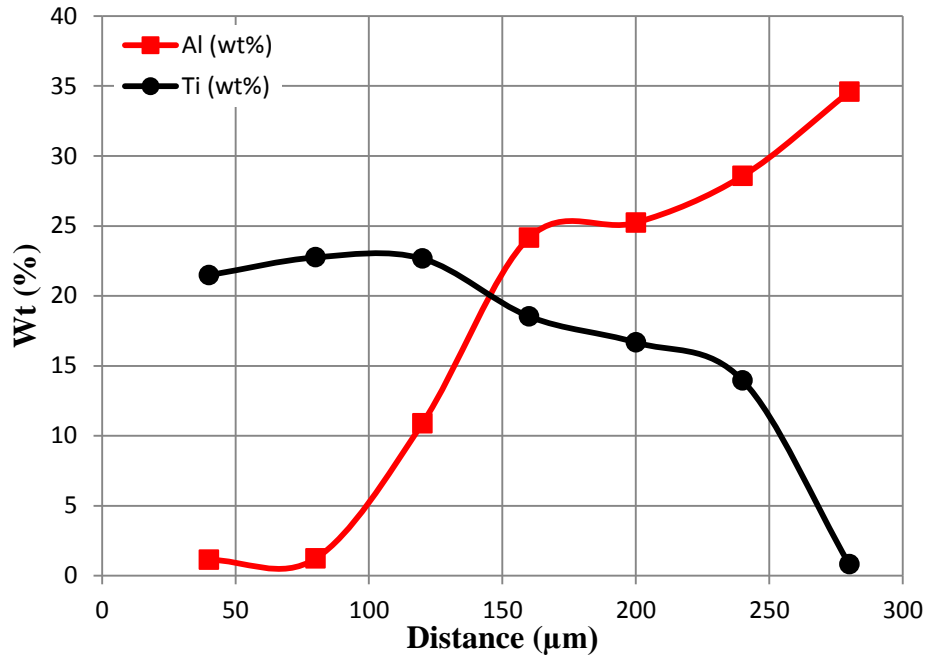
Figure 4.41. EDS line analysis of the sample (CR30F-Plt).

4.4. General Interpretation and Discussion

The Table 4.3 illustrates that metal templates advance how many micrometers diffuse in different alumina powders at 1350°C. According to this, titanium template progress through alumina with diffusing much faster than other metal templates. It is considered that this condition, because of that titanium template, is smooth and direct, in contrast to other templates. On the other hand, it is hard to say that titanium or stainless steel wires which are much faster to diffuse through alumina but copper wire diffuses into alumina lesser than the others.

Table 4.3. Metal templates progress how many μm/hr diffuse in alumina at 1350°C.

Sample	Metal templates diffusion speed (μm/hr at 1350°C)
Ti wire in CT-3000SG	25
Ti wire in AKP50	28
Ti wire in CR6	25,0
Ti wire in CR15	30,0
Ti wire in CR30F	28,0
CR6-Ti	25,0
CR15-Ti	25,0
CR30F-Ti	25,0
CT-3000SG-Plt	27,5
CR30F-Plt	32,5
CR15-St	25,0
CR30F-Cu	0,25

CHAPTER 5

CONCLUSIONS

Densification behavior of the alumina powders was investigated using vertical dilatometers. It is observed that the relative density and densification rate curves of them are similar to each other. There were two distinct peaks at the densification rate versus temperature plots at $1125^{o}C$ for $5^{o}C$/min of heating rate. These two peaks, which belong to alumina CR15 and CR30F, were the densification rate curves of these alumina powders as different from alumina CR6 powder densification behavior. The behavior of relative density of alumina ALCOA is similar to alumina CR6. In addition, the densification rate of alumina AKP50 is higher than that of the other alumina powders. The relative shrinkage, relative density and densification rate of the CR6 alumina powder were investigated at $1500^{o}C$ for 1min. According to the result of this test, it is observed that the relative density of the CR6 increases parabolically and with the densification rate of CR6 is higher than the performed tests for $1350^{o}C$.

BET analysis of the powders indicated surface area values between 4 and 22 m^{2}/g, respectively.

The SEM micrographs of the alumina powders were investigated, and initial particle size of the alumina CR6, CR15 and CR30F powders were finer than 50nm, while the particle size of alumina CT3000SG was finer than 300nm, and alumina AKP50 had an initial particle size of 200nm. Also, EDS analysis of the metal templates were done and it was observed that the metal templates had high purity.

Densification behavior of the alumina samples, which had titanium wire, was investigated using vertical dilatometer. It is understood that the diffusion of titanium into alumina decreases the final density of the samples, while the diffusion of titanium increases the densification rate of the samples at $1350^{o}C$. The titanium wires are still present in the alumina. Titanium proceeded in alumina approximately 100μm at $1350^{o}C$ in four hours of soaking time.

Sintered microstructures of the alumina samples that had Ti wire were investigated from fractured surfaces as well as polished surfaces. It is clear that titanium advanced through alumina about 100μm at $1350^{o}C$ during four hour soaking time. In

addition, the cavity formation is considered to be the result of the Kirkendall effect, where due to the dominating diffusion conditions, the Kirkendall porosity line focuses on the center of the Ti wire rather than at the boundary between the Ti and alumina samples. As a result of EDS analysis of the samples, Al and Ti are seen in the diffusion region, and an intermediate phase of Al_2TiO_5 is formed in the middle of the diffusion region.

According to SEM observation of the alumina samples, which used stainless steel wire, it is noticed that the stainless steel has wholly diffused into the alumina and this diffusion region is approximately 100μm.

Sintered microstructure of the alumina sample, which used copper wire, was examined from polished surfaces. According to EDS analysis of the sample, Al and O is in the alumina matrix while Cu is not. At 1350°C, copper has almost completely melted.

Titanium plate is sandwiched between two alumina pellets in the diffusion couple test and the diffusion after sintering was examined. As a result of SEM observation of the sample, it is observed that approximately 130μm expansion for titanium in alumina occurred while 4 hours soaking time. The Kirkendall porosity by Ti^{+4} diffusing through the fundamentally tough and motionless oxygen sublattice within the TiO_2 and into the surrounding Al_2O_3 without an equal and opposite flux of Al^{+3} to balance it, is probably the reason for observed porosity. In these particular circumstances, the Kirkendall porosity is consolidated into a continuous cavity rather than distributed pores (Goodshaw et al., 2009). Observations of the concentration of Kirkendall porosity into continuous cavities appear to have been first reported by Aldinger (Aldinger, 1974).

In this thesis, the grinding process is not applied to the alumina powders. As a result of this, microcavity formation was not observed after titanium diffusion into alumina. As a further study, if the grinding process is applied to alumina powders for long periods, it can be expected that micro-cavity formation would be provided within the alumina matrix by using titanium templates. In addition to that, the mechanism and kinetics of cavity formation can be investigated further.

REFERENCES

Alcoa, Inc., 2010, Alumina, http://www.alcoa.com.

Aldinger, F., 1973, Controlled porosity by an extreme Kirkendall effect, *Acta Metallurgica*, **22**: p. 923-928.

Baikowski, January 2011, Alumina Technical Information data http://www.baikowski.com.

Besmann, T. M., Kulkami, N. S., Spear, K. E., and Vienna, J. D., 2005, Predicting Phase Equilibria of Spinel-Forming Constituents in Waste Glass Systems, *Journal of the American Ceramic Society*. **168**: p. 121-132.

Bhadeshia, H. K. D. H., December 2011 The Kirkendall effect, http://www.msm.cam.ac.uk/phase-trans/kirkendall.html

Boonyongmaneerat, Y. and Schuh, C. A., 2006, Contributions to the interfacial adhesion in Co-sintered Bilayers, *Metallurgical and Materials Transactions a-Physical Metallurgy and Materials Science*. **37A**(5): p. 1435-1442.

Buscaglia, V., Nanni, P., Battilana, G., Aliprandi, G. and Carry, C., 1994, Reaction sintering of aluminium titanate: I- the effect of MgO addition. *Journal of the European Ceramic Society*. **13**: p. 411-418.

Buscaglia, V., Caracciolo, F., Bottino, C., Leoni, M. and Nanni, P., 1997, Reaction diffusion in the Y_2O_3-Fe_2O_3 system, *Acta Materialia*. **45**(3): p. 1213-1224.

Claussen, N., 1976, Fracture toughness of Al_2O_3 with a stabilized ZrO_2 dispersed phase, *Journal of the American Ceramic Society*. **59**(1-2): p. 49-51.

Collings, E. W., 1994, Materials properties handbook: titanium alloys, ASM International.

Dong, Y., Diwu, J., Feng, X., Liu, X., and Meng, G., 2007, Phase evolution sintering characteristics of porous mullite ceramics produced from the flyash-$Al(OH)_3$ coating powders, *Journal of Alloys and Compounds*. **460**(1): p. 651-657.

Ebbing, D. and Gammon, S. D., 2010, General Chemistry, Cengage Learning.

Emsley, J., 2003, Nature's building blocks: an A-Z quide to the elements, *Oxford University Press*. p. 121-125.

Erol, M., 2008, Ankara üniversitesi KYM345 2007-2008 ders notları BL2. http://chem.eng.ankara.edu.tr/345/345not3.pdf.

Fan, H. J., Knez, M., Scholz, R., Nielsch, K., Pippel, E., Hesse, D., Zacharias, M. and Gösele, U., 2006, Monocrystalline spinel nanotube fabrication based on the Kirkendall effect, *Nature Materials*. **5**: 627-631.

Freudenburg, B. and Mocellin, A., 1987, Aluminum titanate formation by solid state reaction of fine Al_2O_3 and TiO_2 powders, *Journal of the American Ceramic Society*. **70**(1): p. 33-38.

Freudenburg, B. and Mocellin, A., 1988, Aluminum titanate formation by solid state reaction of coarse Al_2O_3 and TiO_2 powders, *Journal of the American Ceramic Society*. **71**(1): p. 22-28.

German R. M. and Park, S. J., 2008, Mathematical relations in particulate materials processing: ceramics, powder metals, cermets, carbides, hard materials, and minerals, John Wiley & Sons. Inc.

Gibson, L. J. and Ashby, M. F., 1986, Cellular solids: structure and properties, Pergamon Press.

Goldenberg, D., 1968, Rev. Int. Hautes Temperature Refract.**5**: p. 181-194.

Goodshaw, H. J., Forrester, J. S., Hanson, R. E., Kisi, E. H. and Suanning, G. J., 2009, Microcavity formation in alumina using Ti templates: formation conditions, *Journal of the American Ceramic Society*. **92**(6): p. 1333-1338.

Hall, B. D., 2008, Powder processing, powder characterization, and mechanical properties of LAST (lead-antimony-silver-tellurium) and LASTT (lead-antimony-silver-tellurium-tin) thermoelectric materials, ProQuest.

Hench, L. L., 1998, Bioceramics, *Journal of the American Ceramic Society*. **81**(7): p. 1705-1728.

Hilman, S. H. and German, R. M., 1992, Constant heating rate analysis of simultaneous sintering mechanisms in alumina, *Journal of Materials Science*. **27**(10): p. 2641-2648.

Huntington, H. B. and Seitz, F., 1942, Mechanism for self diffusion in metallic copper, Phys. Rev. **61**: p. 315-325.

Insaco Inc., 2006, Machining of Hard Materials Alumina 99.9%, http://www.azom.com/article.aspx?ArticleID=3269.

Isobe, T., Tomital, T., Kameshima, Y., Nakajima, A. and Okada, A., 2006, Preparation and properties of porous alumina ceramics with oriented cylindrical pores produced by an extrusion method, *Journal of the European Ceramic Society*. **26**(1): p. 957–960.

Kohl, W. H., 1964, Ceramics and ceramic-to-metal sealing vacuum. **14**(9): p. 333-354.

Kotian, R., 2011, http://shodhganga.inflibnet.ac.in/bitstream/10603/3099/8/08_chapter%202.pdf.

Lautenschlager, E. P. and Monaghan, P., 1993, Titanium and titanium alloys as dental materials, Int. Dent. J. **43**: p. 245-253.

Legros, C., Carry, C., Bowen, P. and Hofmann, H., 1999, Sintering of a transition alumina: Effects of phase transformation, powder characteristics and thermal cycle, *Journal of the European Ceramic Society*. **19**(11): p. 1967-1978.

Leyens, C. and Peters, M., 2003, Titanium and titanium alloys: fundamentals and applications, Wiley-VCH.

Lipowsky, H. and Arpacı, E., 2008, Copper in the automotive industry, John Wiley & Sons.

Liu, G., 2011, Fabrication of porous ceramics and composites by a novel freeze casting, The University of Birmingham.

Low, I. M. and Oo., Z., 2008, In situ diffraction study of self-recovery in aluminium titanate, *Journal of the American Ceramic Society*. **91**(3): p. 1027-1029.

Lowell, S. and Shields, J. E., 1991, Powder surface area and porosity, Siprenger.

Mariotto, S. F. F., Guido, V., Cho, L. Y., Soares, C. P. and Cardoso, K. R., 2011, *Materials Research*. **14**(2): p. 146-154.

Marshall, P., 1984, Austenitic stainless steel: microstructure and mechanical properties, Springer.

McColm, I. J., 1983, Ceramic science for materials technologists. Leonard Hill.

Misra, S. K. and Chaklader, A. C. D., 1963, System copper oxide-alumina, *Journal of the American Ceramic Society*. **46**: p. 509.

Moulson, A. J. and Hebert, J. M., 1990, Electroceramics materials, properties, applications, *Chapman and Hall*. p. 68-76.

Murray, J. L., 1987, Ed., ASM International. p. 1-5.

Nakajima, H., 1997, The discovery and acceptance of the Kirkendall effect: the result of a short research career, JOM. **49**: p. 15-19.

Oocities, December 2011, Metallurgy of steel, http://www.oocities.org/ferritec_eng/chapter_1.htm

Paul, A., 2004, The Kirkendall effect in solid state diffusion, Eindhoven.

Rahaman, M. N., 1995, Ceramic Processing and Sintering, Marcel Dekker.

Ramlee, N. B., 2008, Effect of pH, temperature and chloride concentration on the corrosion behaviour of welded 316L stainless steel, Universiti Technology Malaysia.

Sadowski, T. and Samborski, S., 2007, Development of damage state in porous ceramics under compression. *Computational Materials Science*. **43**(1): p. 75-81.

Sepulveda, P. and Binner, J. G. P., 1999, . Processing of Cellular Ceramics by Foaming and in situ Polymerisation of Organic Monomers. *Journal of the European Ceramic Society.* **19**(1): p. 2059-2066.

Shackelford, J. F. and Doremus, R. H., 2008, Ceramic and glass materials, Springer.

Siao, C. Y., Lee, H. W. and Lu, H. Y., 2009, Kirkendall porosity in barium titanate-strontium titanate diffusion couple, *Ceramic International*. **35**(7): p. 2951-2958.

Silva L. C. C. and Mehl, R. F., 1951, Interface and marker movementsin diffusion in solid solutions of metals, *Trans. AIME*. **191**: p. 155-173.

Silva L. C. C., 1998, A reflection on Mehl R. F. and the Kirkendall effect, *JOM*. **50**: p. 6-7.

Smigelkas, A. D. and Kirkendall E. O., 1947, Zinc diffusion in alpha brass, *Trans. AIME*. **171**: p. 130-134.

Soh, E. and Ruys, A. J., 2009, Characterisation of foamed porous alumina tissue scaffolds, *Journal of Biomimetics*. **4**: p. 21-26.

Sumitomo Chemical, Co. Ltd., 2010, *Alumina*, http://www.sumitomo-chem.co.jp/english/products/index.html.

Tummala, R. R., 1988, Ceramics in microelectronic packaging, *American Ceramic Society Bulletin*. **67**(4): p. 752-758.

Yalamaç, E., 2010, Sintering, Co-Sintering and Microstructure Control of Oxide Based Materials: Zirconia, Alumina, Spinel, Alumina-Zirconia and Spinel-Alumina, Izmir Institute of Technology.